
Kolmogorov-Arnold Energy Models: Fast, Interpretable Generative Modeling

Prithvi Raj^{*1}

Abstract

Generative models typically rely on either simple latent priors (e.g., Variational Autoencoders, VAEs), which are efficient but limited, or highly expressive iterative samplers (e.g., Diffusion and Energy-based Models), which are costly and opaque. We introduce the Kolmogorov-Arnold Energy Model (KAEM) to bridge this trade-off and provide a new avenue for latent-space interpretability. Based on a novel interpretation of the Kolmogorov-Arnold Representation Theorem, which provides new structural biases for generative modeling, KAEM imposes a univariate latent structure that enables fast and exact inference via the inverse transform method. With a low-dimensional latent space and appropriate inductive biases, we show that importance sampling becomes a viable, unbiased, and highly efficient posterior inference method. For settings where importance sampling fails, we propose a population-based strategy that decomposes the posterior into a sequence of annealed distributions to improve mixing during sampling, a common pitfall in Energy-based Models. We evaluate KAEM on SVHN and CelebA, demonstrating potential for promising sample quality when correct inductive biases are chosen, while improving interpretability and inference speed against VAEs.

1. Introduction

Latent variable models generate new data from a low-dimensional latent variable passed through a top-down neural generator. Two prominent examples are Variational Autoencoders (VAEs) (Kingma & Welling, 2022) and Generative Adversarial Networks (GANs) (Goodfellow et al., 2014), where the latent vector is typically drawn from a simple, non-informative prior, such as a uniform or isotropic Gaussian distribution. Latent energy-based models (EBMs) (Pang et al., 2020) offer a more flexible alternative by pa-

rameterizing and learning a data-dependent prior using a neural network, but their practical adoption remains constrained by the need for Langevin Monte Carlo (LMC) sampling (Brooks et al., 2011; Rosky et al., 1978; Roberts & Stramer, 2002). Given its iterative and gradient-based nature, LMC introduces significant computational overhead and mixes poorly in the multimodal latent distributions common to generative modeling. It also introduces additional experimental complexity since the Unadjusted Langevin Algorithm (ULA) is difficult to tune: step sizes that are too small lead to poor mixing and convergence, while larger step sizes can accumulate discretization bias.

Additionally, despite advances in mechanistic interpretability (Bereska & Gavves, 2024), which seeks to reverse engineer neural networks to understand their internal circuitry, there is no established means of interpreting the trained EBM. This forgoes an opportunity to leverage the latent EBM’s explicit separation between prior and generator for discovery and interpretability, particularly in settings where the underlying structure lies on a low-dimensional manifold that can be identified and represented within the latent space, (e.g. Champion et al. (2019)). Such a feature could enable new ways of embedding inductive bias into generative models, similar to the work of Karniadakis et al. (2021), which integrates scientific biases into neural architectures to reduce data dependence and improve training efficiency, generalization, and interpretability, (key requirements for trustworthy Artificial Intelligence).

A key challenge is therefore to design latent priors that (i) admit efficient and stable inference, (ii) expose interpretable structure, and (iii) can be sculpted with domain knowledge rather than learned purely from optimization dynamics. Current latent EBMs fall short because their priors remain neural parameterizations that are difficult to interpret, slow to sample from, and tightly coupled to stochastic, gradient-based, and iterative sampling methods.

We address these requirements by proposing the Kolmogorov-Arnold Energy Model (KAEM), which revises the latent EBM using a collection of univariate energy functions, based on advances in Kolmogorov-Arnold Networks (KANs) (Liu et al., 2024) and deep spline networks (Bohra et al., 2020). By constraining the prior to univariate relationships, KAEM enables interpretability, alongside fast

¹Zettascale Computing Corp.. Correspondence to: Prithvi Raj <prithvi@zsc.ai>.

and exact inference via the inverse transform method for sampling distributions (Devroye, 1986). Additionally, by reinterpreting its inner functions as Markov kernels between probability spaces, we show that KAEM can be viewed as a strict interpretation of the Kolmogorov-Arnold Representation Theorem (KART) (Givental et al., 2009). Given its finite and deterministic structure, KART can be used as a source of structural bias to reduce the reliance of architecture design on intuition and automated tuning.

KAEM is a uniquely robust probabilistic model, and can enable efficient training with importance sampling (IS) (Gortzel, 1949) on simple datasets. This is a technique for estimating posterior expectations that is otherwise avoided in the literature due to its high variance under severe prior-posterior mismatch and the curse of dimensionality, (Dupuis & Wang, 2004), which can be avoided in our model due to the low dimensionality of the latent space. Moreover, we show that the trained priors are easy to visualize and recover, offering new opportunities for latent discovery and knowledge transfer to models with different latent structures.

Our work additionally introduces novel population-based LMC methods (Swendsen & Wang, 1986; Marinari & Parisi, 1992; Hukushima & Nemoto, 1996) to augment posterior sampling for latent EBMs with a sequence of power posteriors (Friel & Pettitt, 2008) and a training criterion derived from Thermodynamic Integration (Calderhead & Girolami, 2009; Annis et al., 2019). Unlike previous attempts at addressing poor convergence and multimodal exploration in EBMs, which typically rely on diffusion-based models (Cui & Han, 2024; Zhang et al., 2023), the proposed population-based training preserves structure, efficiency, and inference speed. This is because our thermodynamic criterion is solely applied during training and scales in parallel over power posteriors, whereas diffusion-based methods scale sequentially with more denoising steps.

Compilation and differentiation were implemented using Julia’s Reactant (EnzymeAD & Reactant.jl Contributors, 2025) and Enzyme (Moses & Churavy, 2020; Moses et al., 2021; 2022) packages, which optimizes and lowers Julia code to Multi-Level Intermediate Representation (MLIR) (Lattner et al., 2020), thus offering best-in-class performance. However, Gaussian Radial Basis Functions (RBF KANs) (Li, 2024), were adopted instead of the cubic B-spline bases used by Liu et al. (2024) for our interpretability experiments, as RBFs are Reactant-compatible and more efficient for GPU implementation. They have also been proven to provide an optimal solution to the regularized approximation/interpolation problem by Poggio & Girosi (1990). For our VAE comparison experiments, wavelet KANs (Bozorgasl & Chen, 2024) were adopted, since they are better suited to LMC methods as they are not constrained by finite and bounded domains, (unlike RBFs without the

grid updating scheme proposed by Liu et al. (2024)).

We evaluate KAEM across several image domains at reduced experimental complexity to demonstrate KAEM’s potential in terms of sample quality and efficiency, as well as the benefit of our proposed training methods. We present KAEM as an initial step to inspire further adaptations of KART in machine learning. This work aims to lay the groundwork for more exploration amongst the research community, with the far-reaching hope of eventually advancing towards a broader conceptualization: “*The Kolmogorov-Arnold Representation Theorem Is All You Need.*”

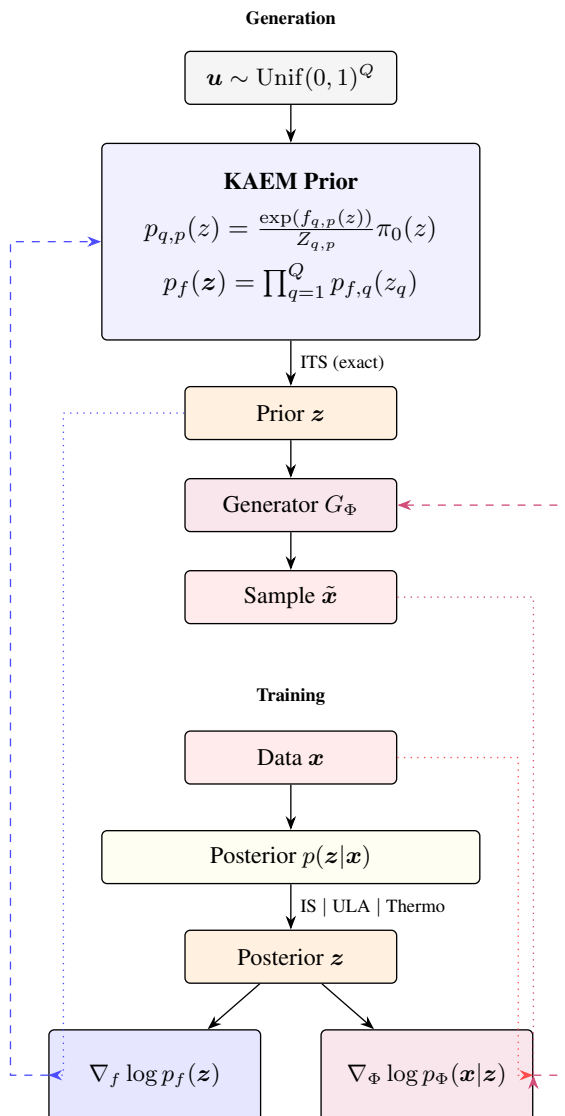


Figure 1. KAEM overview. **Generation:** Inverse transform sampling (ITS) through a mixture prior enables exact latent sampling without Markov chain Monte Carlo (MCMC). **Training:** Posterior inference via importance sampling (fast), Langevin dynamics (fast and exploratory), or Thermodynamic Integration (handles multiple modes) provides samples for parameter gradient updates.

2. Preliminaries

The Kolmogorov-Arnold Representation theorem (KART). Presented by Givental et al. (2009), this forms the basis of KAEM. A structured proof of the theorem has been provided by Dzhenzher & Skopenkov (2022).

Theorem 2.1. For any integer $n_z > 1$, there are continuous univariate functions $\Phi_q : \mathbb{R} \rightarrow \mathbb{R}$ and $\psi_{q,p} : [0, 1] \rightarrow \mathbb{R}$, such that any continuous multivariate function, $g : [0, 1]^{n_z} \rightarrow \mathbb{R}$, can be represented as a superposition of those functions:

$$g(u_1, \dots, u_{n_z}) = \sum_{q=1}^{2n_z+1} \Phi_q \left(\sum_{p=1}^{n_z} \psi_{q,p}(u_p) \right), \quad (1)$$

Latent variable generative models. Let $\mathbf{x} \in \mathcal{X}$ denote observed data vectors and $\mathbf{z} \in \mathcal{Z}$ latent vectors. A top-down generative model specifies

$$p_{\Phi,f}(\mathbf{x}, \mathbf{z}) = p_{\Phi}(\mathbf{x} | \mathbf{z}) p_f(\mathbf{z}), \quad (2)$$

where $p_{\Phi}(\mathbf{x} | \mathbf{z})$ is a neural generator (decoder) and $p_f(\mathbf{z})$ is a latent prior parameterized by f . The log-marginal likelihood is the learning objective for Maximum Likelihood Estimation (MLE):

$$\begin{aligned} \log p_{\Phi,f}(\mathbf{x}) &= \int \log p_{\Phi,f}(\mathbf{x}, \mathbf{z}) p_{\Phi,f}(\mathbf{z} | \mathbf{x}) d\mathbf{z} \\ &= \mathbb{E}_{p_{\Phi,f}(\mathbf{z} | \mathbf{x})} [\log p_{\Phi,f}(\mathbf{x}, \mathbf{z})] \end{aligned} \quad (3)$$

Under Appendix. E.0.3, we prove that the resulting learning gradient exhibits a lack of dependence on sampling:

$$\begin{aligned} \nabla_{\mathbf{x}} \log p_{\Phi,f}(\mathbf{x}) &= \mathbb{E}_{p_{\Phi,f}(\mathbf{z} | \mathbf{x})} \left[\nabla_{\mathbf{x}} [\log p_{\Phi}(\mathbf{x} | \mathbf{z})] \right] \\ &+ \mathbb{E}_{p_{\Phi,f}(\mathbf{z} | \mathbf{x})} \left[\nabla_{\mathbf{x}} [\log p_f(\mathbf{z})] \right]. \end{aligned} \quad (4)$$

Monte Carlo estimator To approximate arbitrary integrals such as the expectation in Eq. 4, one can draw N samples from the target distribution and take an unbiased Monte Carlo estimator. For some arbitrary function, ρ , (e.g., the log-likelihood), the expectation with respect to an arbitrary density, p , can be estimated as:

$$\begin{aligned} \mathbb{E}_{p(z)}[\rho(z)] &= \int_{\mathcal{Z}} \rho(z) p(z) dz \approx \frac{1}{N} \sum_{s=1}^N \rho(z^{(s)}), \\ \text{where } \{z^{(s)}\}_{1:N} &\sim p(z). \end{aligned} \quad (5)$$

Top-down generator The latent-to-data generative process is realized using a neural network $G_{\Phi} : \mathcal{Z} \rightarrow \mathcal{X}$, (parameterized by Φ), which maps a latent sample z to a reconstruction (mean image or data sample)

$$\tilde{\mathbf{x}} = \mu_{\Phi}(\mathbf{z}) = G_{\Phi}(\mathbf{z}) + \varepsilon, \quad \varepsilon \sim \mathcal{N}(\mathbf{0}, \sigma_{\text{noise}} \mathbf{I}), \quad (6)$$

In this work we model the conditional likelihood with an isotropic Gaussian observation model, equivalent to a pixel-wise ℓ_2 reconstruction objective:

$$p_{\Phi}(\mathbf{x} | \mathbf{z}) = \mathcal{N}(\mathbf{x}; \mu_{\Phi}(\mathbf{z}), \sigma_x^2 \mathbf{I}), \quad (7)$$

where σ_x^2 is a specified variance, σ_{noise}^2 captures observation noise, and \mathbf{I} is the identity matrix over pixels and channels. For an image $x \in \mathbb{R}^{H \times W \times C}$, the corresponding log-likelihood is

$$\log p_{\Phi}(\mathbf{x} | \mathbf{z}) \propto -\frac{1}{2\sigma_x^2} \|\mathbf{x} - \mu_{\Phi}(\mathbf{z})\|_2^2 \quad (8)$$

Up to an additive constant, maximizing $\log p_{\Phi}(\mathbf{x} | \mathbf{z})$ is equivalent to minimizing the pixel-wise squared error. The gradient needed for the log-likelihood component of Eq. 4 can then be found by autodifferentiation, which we used Enzyme (Moses & Churavy, 2020) for.

Latent energy-based prior. Latent EBMs (Pang et al., 2020) define the prior by an energy E_f and base reference prior, e.g., $\pi_0 = \mathcal{N}(0, 1)$:

$$p_f(\mathbf{z}) \propto \exp(E_f(\mathbf{z})) \cdot \pi_0(\mathbf{z}). \quad (9)$$

Training requires sampling from the posterior

$$p_{\Phi,f}(\mathbf{z} | \mathbf{x}) \propto p_{\Phi}(\mathbf{x} | \mathbf{z}) p_f(\mathbf{z}), \quad (10)$$

which is often multimodal and difficult to sample from.

Unadjusted Langevin Algorithm (ULA). Given a target $\pi(z) \propto \exp(\log \pi(z))$, ULA (Brooks et al., 2011) iterates

$$z^{i+1} = z^i + \frac{\eta}{2} \nabla_z \log \pi(z^i) + \sqrt{\eta} \xi^i, \quad \xi^i \sim \mathcal{N}(0, I), \quad (11)$$

with step size $\eta > 0$. In latent EBMs, π is either the prior (9) or posterior (10). ULA is best suited to sampling from unimodal distributions. Following Pang et al. (2020) we adopt a small iteration count, (40 iterations), following the guidance of Nijkamp et al. (2019b;a) regarding short-run Markov chain Monte Carlo, and to limit the resource expenditure of our experiments.

Power posteriors. To improve mixing, KAEM samples from *power posteriors* (Friel & Pettitt, 2008):

$$p_{\Phi,f,t}(\mathbf{z} | \mathbf{x}) \propto p_{\Phi}(\mathbf{x} | \mathbf{z})^t p_f(\mathbf{z}), \quad t \in [0, 1], \quad (12)$$

where $t = 0$ recovers the prior and $t = 1$ recovers the posterior. A population of chains at $\{t_k\}_{k=0}^K$ with swap moves (parallel tempering) improves exploration. Thermodynamic Integration connects expectations under p_{t_k} to log-normalizer differences; details are deferred to Sec. 3.2.

3. Method

3.1. Architecture

KAEM prior. The inner functions, $\psi_{q,p}$, of Therorm 1 can be conveniently translated to the framework of inverse transform sampling (ITS) (Devroye, 1986). We interpret $\psi_{q,p}$ as the application of an inverse cumulative density function (CDF) to a uniform random variable to recover a sample from a univariate latent density, $p_{q,p}$:

$$z = \psi_{q,p}(u_p) = F_{\pi_{q,p}}^{-1}(u_p) \Leftrightarrow z \sim p_{q,p}(z). \quad (13)$$

Here, $F_{\pi_{q,p}}^{-1} : [0, 1] \rightarrow \mathcal{Z}$ is the generalized inverse CDF associated with a parameterized latent measure, $\pi_{q,p}$ in the latent space. Since $F_{\pi_{q,p}}^{-1}$ is a measurable, monotone, increasing function, it can be viewed as a Markov kernel between two probability spaces and does not invalidate the deterministic structure of KART. We discuss and formalize this in more detail in Appendix. B.1. We adapt the formulation of Pang et al. (2020) to the univariate case, and parameterize the latent density via exponential tilting of a base prior π_0 :

$$p_{q,p}(z) = \frac{\exp(f_{q,p}(z))}{Z_{q,p}} \pi_0(z), \quad (14)$$

where $f_{q,p}(z)$ is a learned energy function and $Z_{q,p}$ is the finite normalizing constant (partition function) that ensures validity in the defined density. In our method, we parameterize the functions, $f_{q,p}$, using Radial Basis Functions (RBFs) (Li, 2024) or wavelets (Bozorgasl & Chen, 2024).

Given the independence of the prior’s parameters, the log-prior can be modeled as a sum over the univariate cases:

$$\begin{aligned} \log p_f(z) &= \sum_{q=1}^Q \sum_{p=1}^P \log p_{q,p}(z_{q,p}) \\ &= \sum_{q=1}^Q \sum_{p=1}^P f_{q,p}(z_{q,p}) + \log \pi_0(z_{q,p}) - \log Z_{q,p}, \end{aligned} \quad (15)$$

where $P = n_z, Q = 2n_z + 1$ are taken throughout the study based on the structure of KART in Eq. 1. Following the approach of Pang et al. (2020) we adopt the contrastive divergence (CD) criterion to train the univariate prior. This is derived under Appendix. E.0.4:

$$\begin{aligned} \mathbb{E}_{p_{f,\Phi}(z|\mathbf{x})} \left[\nabla_f [\log p_f(z)] \right] &= \\ \mathbb{E}_{p_{f,\Phi}(z|\mathbf{x})} \left[\nabla_f \sum_{q=1}^{2n_z+1} \sum_{p=1}^{n_z} f_{q,p}(z) \right] &= \\ - \mathbb{E}_{p_f(z)} \left[\nabla_f \sum_{q=1}^{2n_z+1} \sum_{p=1}^{n_z} f_{q,p}(z) \right]. \end{aligned} \quad (16)$$

We approximate these expectations with Monte Carlo estimators after first drawing samples from the prior using ITS, and from the posterior using ULA or population-based sampling. Alternatively, posterior sampling can be circumvented entirely using the importance sampling (IS) estimator. Similar to the log-likelihood in Eq. 8, the gradients can be found with autodifferentiation.

KAEM mixture-of-univariate prior. The form in Eq. 14 ignores inter-dimensional dependencies in the latent space and results in an axis-aligned joint distribution. For efficiency and scalability, we can also parameterize the latent as $z \in \mathbb{R}^Q$ (we write z_q for the q -th coordinate) and defines a mixture prior per coordinate, where $f_{q,p}$ is realized as univariate KAN or spline functions.

$$p_f(z) = \prod_{q=1}^Q p_{f,q}(z_q), \quad p_{f,q}(z) = \sum_{p=1}^P \alpha_{q,p} p_{q,p}(z), \quad (17)$$

where $\alpha_{q,p} \geq 0$ and $\sum_p \alpha_{q,p} = 1$. Sampling becomes more efficient than in the previous formulation 14, as it proceeds component-wise using ITS for discrete variables, (Devroye, 2006). However, this violates KART, since $F_{\pi_{q,p}}^{-1}$ now corresponds to a discrete rather than a continuous CDF.

Here, $\alpha_{q,p}$ are mixture proportions, which must satisfy non-negativity and unit-sum constraints. They could be fixed uniformly as $1/n_z$, guided by (Rivera, 2024). However, in this study, they were learned by passing trainable parameters through a softmax function, (to enforce the constraints). A small regularization term, (the summed absolute value of all $\alpha_{q,p}$, scaled by $\lambda = 0.0001$), was incorporated into the loss to encourage uniformity.

Deriving a CD learning gradient for the mixture prior is less direct than in the fully factorized univariate case, due to the presence of log-sum-exp mixture coupling. However, each component admits a tractable one-dimensional partition function, therefore the prior component to the learning gradient in Eq. 4 can be evaluated directly, without requiring

CD. In particular, the mixture log-density takes the form

$$\log p_f(\mathbf{z}) = \sum_{q=1}^Q \log \text{sumexp}_p \left(\log \alpha_{q,p} + f_{q,p}(z_q) + \log \pi_0(z_q) - \log Z_{q,p} \right), \quad (18)$$

where $Z_{q,p}$ is found by quadrature, (Eq. 20). Automatic differentiation can then be used to compute the gradient $\nabla_f \log p_f(\mathbf{z})$, required for training with Eq. 4.

Generator Having sampled the intermediary latent variable with ITS such that $z_{q,p} = F_{\pi_{q,p}}^{-1}(u_p)$, the top-down generation is realized flexibly using Eq. 6, where $G_\Phi : \mathcal{Z} \rightarrow \mathcal{X}$ is a neural network parameterized by Φ :

$$G_\Phi(\mathbf{z}), \quad \text{where } \mathbf{z} = \{z_{q,p}\}_{1:Q,1:P} \quad (19)$$

In this study, we primarily use convolutional neural networks (CNNs) (LeCun et al., 2015) due to their spatial inductive bias: sequences of convolutional layers implement shift-equivariant transformations that are well-suited for images. However, we also consider using Kolmogorov-Arnold Networks (KANs) for simple datasets and strict adherence to KART (Eq. 1). This is discussed under Appendix. B.2.

The log-likelihood in Eq. 8 can be differentiated to train the generator, as per Eq. 4 for the posterior expectations. These expectations can be approximated either with the standard Monte Carlo estimator in Eq. 5, or with the importance sampling (IS) estimator, which circumvents the need to sample from the posterior.

3.2. Sampling

Normalization and inverse transform. Since $Z_{q,p}$ is one-dimensional, it can be computed efficiently by Gauss-Kronrod quadrature, (Laurie, 1997):

$$Z_{q,p} = \int_{z_{\min}}^{z_{\max}} \exp(f_{q,p}(z)) \pi_0(z) dz \approx \sum_{i=1}^{N_{\text{quad}}} w_i, H(z_i^{\text{node}}), \quad (20)$$

where $H(z) = \exp(f_{q,p}(z)) \pi_0(z)$, and $\{z_i^{\text{node}}, w_i\}_{i=1}^{N_{\text{quad}}}$ are the quadrature nodes and weights for the interval $[z_{\min}, z_{\max}]$. The availability of $Z_{q,p}$ enables inverse transform sampling (ITS) from the prior, and the smoothness of H , together with its bounded support, makes this approximation accurate.

The multivariate latent product density, (Eq. 17), is exact-sampleable since each $p_{q,p}$ is univariate and normalized. Sampling from the mixture proceeds by selecting $p^* \sim \text{Cat}(\alpha_{q,1:P})$ and then sampling $z_q \sim p_{q,p^*}$ via ITS. Algorithm 1 summarizes the procedure. To sample from Eq. 14, one simply has to skip component-selection and sample from all densities, $p_{1:Q,1:P}$.

Algorithm 1 Exact sampling from KAEM mixture prior by inverse transform sampling (ITS)

Require: Weights $\alpha_{q,1:P}$, energies $f_{q,1:P}$, base density π_0 , Gauss-Legendre nodes and weights $\{z_i, w_i\}_{i=1}^N$.

Ensure: Sample $z \in \mathbb{R}^Q$ from $p_f(\mathbf{z})$.

- 1: **for** $q = 1$ to Q **do**
 - 2: **Sample component** $p^* \sim \text{Categorical}(\alpha_{q,1:P})$.
 - 3: **Find** $Z_{q,p} \leftarrow \sum_{i=1}^N w_i \exp(f_{q,p^*}(z_i)) \pi_0(z_i)$.
 - 4: **CDF table:** $C_0 \leftarrow 0$ and $C_i \leftarrow C_{i-1} + w_i \exp(f_{q,p^*}(z_i)) \pi_0(z_i)$.
 - 5: **Normalize:** $C_i \leftarrow C_i / Z_{q,p} \quad \forall i$.
 - 6: **Sample** $u \sim \text{Unif}(0, 1)$.
 - 7: **Find bin:** Smallest j such that $C_j \geq u$.
 - 8: **Interpolate:** $t \leftarrow \frac{u - C_{j-1}}{C_j - C_{j-1}}, z_q \leftarrow (1-t)z_{j-1} + tz_j$.
 - 9: **end for**
 - 10: **return** z .
-

Importance sampling (IS) We can estimate expectations with respect to $p_{f,\Phi}(\mathbf{z} | \mathbf{x})$ using importance sampling (IS) (Kloek & van Dijk, 1978) with the prior as proposal. Algorithm 2 summarizes the procedure. More details are provided under Appendix. C, including theoretical depth regarding the importance weights, and a summary of residual resampling, which we adopt for variance reduction and to focus learning on samples that are more representative of the posterior distribution.

IS is used to estimate the log-marginal likelihood and its gradient in Eq. 4. However, unlike ULA (Eq. 11), IS fails to support posterior exploration when the prior is poorly aligned, making it unsuitable for general-purpose tasks beyond those similar to the NIST datasets. In cases where IS fails, we can adopt ULA to sample from $p_{f,\Phi}(\mathbf{z} | \mathbf{x})$ and estimate MLE’s posterior expectation in Eq. 3 using the standard Monte Carlo estimator in Eq. 5.

Thermodynamic criterion and population-based ULA

To mitigate the poor convergence of ULA with multimodal posterior landscapes, we introduce a training criterion that facilitates posterior annealing. Details on the cyclic annealing schedule adopted in this study, along with practical guidance on hyperparameter selection, are provided in Sec. D.

We inform our derivations using the Thermodynamic Integral, derived in Sec. E.0.5. In place of the log-marginal likelihood of Eq. 3, this uses the power posterior in Eq. 12:

$$\log(p_{f,\Phi}(\mathbf{x})) = \int_0^1 \mathbb{E}_{p_{f,\Phi}(\mathbf{z} | \mathbf{x}, t)} [\log(p_\Phi(\mathbf{x} | \mathbf{z}))] dt \quad (21)$$

The exact calculation of the integral in Eq. 21 is feasible given that the bounds are $t = 0$, corresponding to the expectation being taken with respect to the prior, and $t = 1$,

Algorithm 2 Posterior expectation via importance sampling

Require: Observation $\mathbf{x}^{(s)}$, prior $p_f(\mathbf{z})$, likelihood $p_\Phi(\mathbf{x} | \mathbf{z})$, number of samples N , ESS threshold $\gamma \in (0, 1)$.

Ensure: Approximation of $\mathbb{E}_{p_{f,\Phi}(\mathbf{z}|\mathbf{x})}[\rho(\mathbf{z})]$.

- 1: **Sample proposal:** Draw $\{\mathbf{z}^{(s)}\}_{1:N} \sim p_f(\mathbf{z})$ using inverse transform sampling (Algorithm 1).
- 2: **Find importance weights using the likelihood:**

$$w^{(s)} \leftarrow p_\Phi(\mathbf{x} | \mathbf{z}^{(s)}), \quad w_{\text{norm}}^{(s)} \leftarrow \frac{w^{(s)}}{\sum_{r=1}^N w^{(r)}}$$

implemented stably via a softmax over $\log w^{(s)}$.

- 3: **Effective sample size (ESS):**

$$ESS \leftarrow \frac{1}{\sum_{1:N} (w_{\text{norm}}^{(s)})^2}.$$

- 4: **if** $ESS < \gamma N$ **then**
- 5: **Resample:** Resample $\{\mathbf{z}'^{(s)}\}$ according to $w_{\text{norm}}^{(s)}$ (we use residual resampling; Sec. C.2).
- 6: Set $w_{\text{norm}}^{(s)} \leftarrow 1/N$.
- 7: **end if**
- 8: **Estimate expectation:**

$$\mathbb{E}_{p_{f,\Phi}}[\rho(\mathbf{z})] \approx ; \sum_{s=1}^N w_{\text{norm}}^{(s)} \rho(\mathbf{z}^{(s)}) \approx \frac{1}{N} \sum_{s=1}^N \rho(\mathbf{z}'^{(s)}).$$

- 9: **return** estimated expectation.

where it is taken with respect to the posterior. However, the integral can also be expressed exactly without collapsing the temperatures. This allows greater flexibility in how the integral evolves through the temperature schedule, $\{t_k\}_{k=0}^{N_t}$. In particular, the temperature schedule is discretized as:

$$t = \{t_0, t_1, \dots, t_{N_t}\}, \quad t_k \in [0, 1] \quad (22)$$

In Sec. E.0.7, the Steppingstone estimator (SE) introduced by Annis et al. (2019) is derived from the discretized Thermodynamic Integral presented by Calderhead & Girolami (2009), (and provided under Sec. E.0.6). This establishes a connection between the two, which we use to derive the learning gradient and inform our approach to the clustering the temperatures in Eq. 22:

$$\begin{aligned} \log p_{f,\Phi}(\mathbf{x}) &= \sum_{k=1}^{N_t} \log \frac{Z_{t_k}}{Z_{t_{k-1}}} \\ &= \sum_{k=1}^{N_t} \left(\log Z_{t_k} - \log Z_{t_{k-1}} \right) = \underbrace{\log Z_{t_{N_t}}}_{=\text{MLE}} - \underbrace{\log Z_{t_0}}_{=0 \text{ (Eq. 41)}}. \end{aligned} \quad (23)$$

The log-partition ratios are estimated with Monte Carlo estimators using all annealed samples:

$$\begin{aligned} \log p_{f,\Phi}(\mathbf{x}) &= \log Z_{t_{N_t}}^{\text{SS}} = \sum_{k=1}^{N_t} \log \left(\frac{Z_{t_k}}{Z_{t_{k-1}}} \right) \\ &\approx \frac{1}{N} \sum_{k=1}^{N_t-1} \sum_{s=1}^N (t_{k+1} - t_k) \left[\log p_\Phi(\mathbf{x} | \mathbf{z}^{(s, t_k)}) \right], \end{aligned}$$

where $\underbrace{\{\mathbf{z}\}_{1:N, 1:N_t} \sim p_{f,\Phi}(\mathbf{z} | \mathbf{x}, t_k)}_{\text{population-based ULA}}, \quad (24)$

where (s, t_k) indexes the sample and temperature. SE and its variants, such as Annealed Importance Sampling (AIS) (Neal, 1998), are commonly used to estimate a model's evidence without a tractable way to learn the prior, as they lack dependence on prior gradients beyond sampling. However, by recognizing the direct connection between the SE and MLE learning gradients, as proven in Sec. E.0.7, one can simply add the prior expectation from Eq. 4 to Eq. 24.

This is valid because the SE gradient matches the MLE gradient, and the likelihood gradient is independent of the prior gradient. The posterior expectation of the log-prior in Eq. 4 can be estimated with a Monte Carlo estimator using the final samples of ULA for either contrastive divergence in Eq. 16 or the normalized mixture log-prior in Eq. 18.

Population-based ULA In their implementation of Thermodynamic Integration, Calderhead & Girolami (2009) estimated the Thermodynamic Integral with the discretization in Sec. E.0.6, using population-based Markov-chain Monte Carlo (MCMC) and Parallel Tempering (PT) (Swendsen & Wang, 1986; Marinari & Parisi, 1992; Hukushima & Nemoto, 1996) to sample from all power posteriors.

Specifically, parallel chains were simultaneously maintained at each temperature, (or Replica), using Metropolis-Hastings (MH) (Metropolis & Ulam, 1949), to drive local moves for each power posterior. They also proposed a geometric path between the prior and posterior, enabling global swaps between adjacent temperatures. This approach allowed higher temperatures to leverage the efficient mixing of lower temperatures, thereby facilitating a more thorough exploration of the posterior landscape.

We adopt a similar strategy but follow Pang et al. (2020) in using ULA, (Eq. 11), to drive local moves within each Replica without MH correction. Annealing with power posteriors can improve ULA against multimodal posterior landscapes. Mixing can be further improved by swapping populations between randomly selected adjacent temperatures, subject to:

$$r = \frac{p_\Phi(\mathbf{x} | \mathbf{z}^{(i, t_{k+1})})^{t_k} p_\Phi(\mathbf{x} | \mathbf{z}^{(i, t_k)})^{t_{k+1}}}{p_\Phi(\mathbf{x} | \mathbf{z}^{(i, t_k)})^{t_k} p_\Phi(\mathbf{x} | \mathbf{z}^{(i, t_{k+1})})^{t_{k+1}}}, \quad (25)$$

where (i, t_{k+1}) indexes the ULA iteration and temperature, and the proposed swap, $z^{(i, t_{k+1})} \leftrightarrow z^{(i, t_k)}$, is accepted with probability: $\min(1, r)$. In this study, we perform this check every iteration, for a randomly chosen adjacent pair of power posteriors.

4. Experiments

4.1. Setup

Scope We first show that importance sampling becomes a viable and highly efficient training strategy for simple NIST (Deng, 2012; Xiao et al., 2017) datasets, due to the low dimensionality of the latent space. We also demonstrate that the model remains effective when strictly adhering to KART with independent energy-based priors, thereby validating the use of KART as a source of structural inductive bias. Additionally, we plot a single learned distribution to demonstrate KAEM’s interpretability. Architectures and hyperparameter details are provided in Table 4.

We subsequently evaluate the mixture EBM prior against SVHN (32×32) (Netzer et al., 2011) and CelebA (64×64) (Liu et al., 2015), sampled via component-wise ITS and paired with CNN-decoder architectures, which are slightly smaller variants of those used by Pang et al. (2020). We additionally compare KAEM trained using single-posterior ULA sampling with the MLE criterion against a population-based ULA sampling strategy using the thermodynamic criterion. These comparisons assess the practicality of using mixture densities for scaling KAEM and using annealing to improve training for high-dimensional RGB images. Hyperparameters are provided in Table 5. Architectural details for KAEM and the baseline VAE are provided under Appendix F.2.

Benchmarks Benchmarks were collected for KAEM and the VAE baseline in FP32 on a GPU (NVIDIA GeForce RTX 4060) with Julia’s BenchmarkTools package, (JuliaCI, 2024). Compilation and reverse differentiation were performed using Julia’s Reactant (EnzymeAD & Reactant.jl Contributors, 2025) and Enzyme (Moses & Churavy, 2020; Moses et al., 2021; 2022) packages. They reflect a reverse autodifferentiation of the training criteria in Eqs. 4, 24, or the prior sampling process during inference.

Image metrics To quantify the fidelity of generated data in a more reliable manner than previous generative modeling studies, we used effectively unbiased metrics based on the ideas outlined by Chong & Forsyth (2020). By applying linear regression to extrapolate the values of standard metrics to an infinitely sized sample set, Monte Carlo error was mitigated, (otherwise associated with finite sample sizes).

For SVHN and CelebA, we gathered $\overline{\text{FID}}_\infty$ and $\overline{\text{KID}}_\infty$, which are effectively unbiased estimators of the Fréchet In-

ception Distance and Kernel Inception Distance, by Heusel et al. (2018); Bińkowski et al. (2021) respectively. The set of sample sizes used for linear regression were: 2000, 4000, 6000, 8000, 10000, 12000, 14000, 16000, 18000, 20000.

However, we recognize that quantifying the fidelity of generated data is challenging and not an exact science. While the metrics used in this study have limitations, they align with those commonly found in the literature. Our conclusions are also informed by our subjective perception of the images. Furthermore, no metrics were applied for the NIST datasets, as vision metrics rely on the Inception V3 model trained on ImageNet (Szegedy et al., 2015), potentially introducing bias against other datasets, especially non-RGB images.

Generated samples can be found in Appendix. G. The main body solely presents results for our conclusions.

4.2. Results

MNIST & FMNIST KAEM was trained on the MNIST and FMNIST (Deng, 2012; Xiao et al., 2017) datasets for 10 epochs with 50,000 training examples, an importance sample and batch size of $N = 100$, (corresponding to 5,000 parameter updates). Prior sampling proceeded by ITS and posterior expectations were estimated with IS. The architecture was guided strictly by KART, using the KAN generator in Appendix B.2. Univariate functions were realized with RBFs (Li, 2024) and independent priors were used.

KAEM consistently generated a diverse set of samples when non-restrictive reference priors were used, (Gaussian, uniform, or no reference, plotted in Appendix G.1), thus validating importance sampling, independent energy-based priors, and strict adherence to KART for simple datasets.

Fig. 3 depicts a single latent component of KAEM trained on FMNIST with a Gaussian reference prior, demonstrating KAEM’s potential for latent prior discovery. Generally, priors were modified minimally when trained with IS, they remained largely aligned with the references. This suggests that the reference prior used to initialize KAEM guides the structure of the resulting latent space and may provide a useful source of inductive bias or reusable structure.

SVHN and CelebA We evaluated KAEM using a CNN generator against RGB datasets at different resolutions, SVHN (32×32) (Netzer et al., 2011) and CelebA (64×64) (Liu et al., 2015). Training was shortened to 40,000 parameter updates, (70,000 were used in the study by Pang et al. (2020)), and smaller variants of the CNN decoder architectures used by Pang et al. (2020) were adopted as the generators. Instead of RBFs, univariate functions were realized using Morelet wavelets (Bozorgasl & Chen, 2024).

A single optimizer (Adam) was used to train both models, rather than using separate optimizers for the prior and

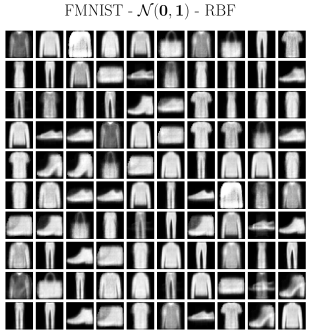


Figure 2. Generated FMNIST using a Gaussian reference prior

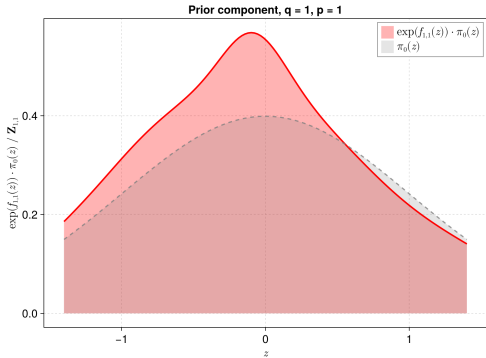


Figure 3. Component $p_{q=1, p=1}(z)$ after training on FMNIST. The density has been normalized by $Z_{q=1, p=1}$ using quadrature, however there is a small discretization bias preventing exactness.

generator. Full architectural details are provided under Appendix 3.1. Posterior sampling was conducted with 40 steps of ULA, and a standard Gaussian reference prior was used, $\pi_0 = \mathcal{N}(0, 1)$. KAEM was trained for 200 epochs with a batch size of $N_x = 100$ on 20,000 training examples. All remaining hyperparameters are in Tab. 5. Annealing was conducted with $N_t = 5$ power posteriors and the p scheduling outlined in Sec. D.1.

We note that sample quality is sensitive to the prior architecture. In Appendix H, we report a smaller-scale experiment using RBF bases instead of wavelets, which resulted in higher-quality samples after just 16,000 parameter updates. This architecture is more promising against VAEs

Our small mixture prior model was able to generate low-quality samples on both SVHN and CelebA, demonstrating the potential of component-wise ITS for exact and highly efficient prior sampling, as an alternative to the iterative and biased approach of Pang et al. (2020). Full computational benchmarks for the architectures and hyperparameters for SVHN (32×32) are provided in Appendix A, demonstrating that KAEM samples faster than the baseline VAE, (despite requiring more memory). We believe this is due to the slight architectural differences noted in Fig. 4.

Table 1. Effectively unbiased FID and KID scores (lower is better) for SVHN (32×32), with regression metrics.

Model	FID			KID		
	Value	Std. Err.	R^2	Value	Std. Err.	R^2
MLE	97.61	0.105	0.976	0.0930	0.00021	0.411
Thermo	148.84	0.093	0.971	0.1363	0.00016	0.091
VAE	62.83	0.160	0.959	0.0532	0.00018	0.560

Table 2. Effectively unbiased FID and KID scores (lower is better) for CelebA (64×64), with regression metrics.

Model	FID			KID		
	Value	Std. Err.	R^2	Value	Std. Err.	R^2
MLE	251.64	0.176	0.949	0.2687	0.00037	0.418
Thermo	165.62	0.152	0.962	0.1815	0.00021	0.019
VAE	113.33	0.113	0.974	0.1152	0.00013	0.591

Our proposed thermodynamic strategy led to worse image metrics on SVHN, (and both datasets in Appendix H), but enabled KAEM to escape posterior collapse to a single mode when trained on CelebA. As shown in Appendix G.2, training with ULA and MLE produced degenerate CelebA samples, whereas population-based methods successfully mitigated this failure mode.

Subjectively, images generated under thermodynamic training appeared more well-defined (i.e., lower variance), but were less diverse than under MLE. Future work could investigate prior parameterized by functions other than wavelets, as well as the regimes in which thermodynamic training is preferable to MLE. While SVHN performed better under the MLE objective, CelebA appeared to benefit subjectively from thermodynamic training, producing more human-perceptible features in both experiments, wavelets and RBFs. For instance, a better tuned annealing schedule may sharpen SVHN features similar to CelebA in Fig. 18.

Ultimately, we cannot justify the thermodynamic strategy due to its substantial computational overhead. With greater VRAM availability, it would be possible to parallelize a larger number of temperatures than the $N_t = 5$ used in this study, which could potentially improve sample quality, as suggested by the results of Calderhead & Girolami (2009).

Alternatively, different posterior sampling approaches, such as other annealing schedules, more ULA steps, or the use of autoMALA (Biron-Lattes et al., 2024) with bias correction and temperature-adaptive step-size tuning, may further improve performance. However, exploring these options might not be worthwhile until the hardware described by Zettascale Computing Corporation (2026) becomes available, given the added algorithmic complexity, hyperparameter sensitivity, and extended training times involved.

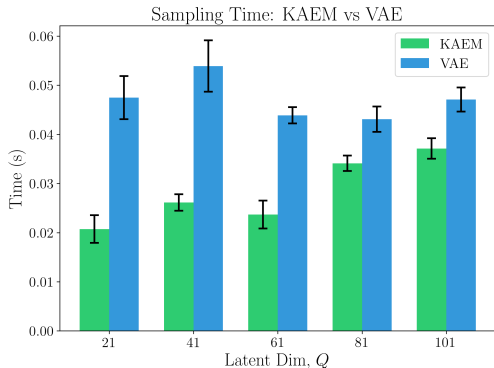


Figure 4. Sampling (inference) times of KAEM and VAE across latent dimensionality, Q . KAEM uses inverse transform sampling (ITS) from the EBM prior, while VAE decodes from $z \sim \mathcal{N}(\mathbf{0}, \mathbf{I})$. Error bars correspond to standard deviation. We believe that the VAE is slower because it includes a dense projection layer before the convolutional decoder, while KAEM’s generator operates directly on the reshaped latent representation (see F.2).

Another direction for posterior inference could involve amortized approaches similar to Kingma & Welling (2022), particularly since the VAE consistently outperformed KAEM. The information bottleneck criterion has previously been derived for latent EBMs by Kong et al. (2021).

5. Conclusions

KAEM provides a principled framework for structured and interpretable generative modeling. Our results demonstrate that importance sampling enables efficient training on simple or low-dimensional datasets, while the Kolmogorov-Arnold Representation Theorem offers a principled basis for architectural design, allowing KAEM’s structure to be determined entirely by its latent space dimensionality. The inverse transform method provides clear advantages over Langevin Monte Carlo for sampling energy-based priors, offering both speed and exactness. While the benefits of annealing and population-based posterior sampling remain inconclusive in our experiments, these directions warrant further investigation as hardware capabilities continue to advance, particularly with developments such as those introduced by Zettascale Computing Corporation (2026).

5.1. Future work

Hardware acceleration Benchmarks are in Appendix A, compiled using Reactant (EnzymeAD & Reactant.jl Contributors, 2025) and EnzymeMLIR for automatic differentiation (Moses & Churavy, 2020; Moses et al., 2021; 2022).

The univariate, localized nature of B-spline interpolations complicates their parallelization on GPUs due to sparse and recursive computations, so RBF and wavelet bases were used instead. The search operations needed for inverting the

cumulative density functions, categorical sampling from the mixture, and residual resampling (Algorithms 1 & 3), were also difficult to parallelize as GPUs are generally ill-suited for search algorithms that rely on conditional logic. Parallelizing conditionals leads to thread divergence, making GPUs inefficient for these operations. To compile the model with Reactant, these algorithms were implemented using sparse multiplications for conditional masking, which was functional but suboptimal on GPUs.

Moreover, while ITS enables fast and scalable inference for mixture priors, KAEM’s training with ULA does not scale efficiently on GPUs due to the iterative, gradient-based nature of Langevin dynamics. GPUs are poorly suited to Langevin methods because of irregular memory access patterns and bandwidth pressure from differentiating with respect to inputs, which requires storing intermediate outputs across generator layers.

However, Zettascale Computing Corporation (2026) introduces the XPU, a reconfigurable dataflow accelerator designed for highly efficient parallel execution, differentiation, and reduction of univariate nonlinear functions. The reconfigurable dataflow architecture is particularly well-suited to KAEM’s computational patterns, offering precise data flow control that mitigates challenges from unstructured sparsity and irregular memory access.

The XPU is especially promising for accelerating KAEM’s univariate structure and sampling operations, but it also presents a path toward more efficient ULA implementations and improved posterior sampling, potentially enabling bias correction and adaptive step-size tuning with autoMALA (Biron-Lattes et al., 2024), which is desirable when a single step size proves insufficient across power posterior geometries. Even without annealing, replacing ULA with autoMALA may yield a more robust probabilistic model with stronger theoretical guarantees.

KAEM may ultimately prove more scalable than conventional generative models due to its reliance on finite representations of continuous functions and its compatibility with the XPU architecture.

Expanding the role of importance sampling For SVHN and CelebA, IS proved infeasible as a posterior sampler, necessitating ULA for the RGB image datasets. While IS is limited by estimator variance, ULA is constrained by mixing difficulties when sampling multimodal distributions (addressed here through annealing).

The failure of IS on more complex datasets likely stems from prior-posterior mismatch, which renders the IS estimator ineffective. Furthermore, IS restricts the prior to its initial domain, since proposals are generated via ITS using finite-domain KAN energy functions. In contrast, ULA can

explore beyond this domain, enabling adaptation through the grid-updating scheme proposed by Liu et al. (2024).

One potential remedy for the curse of dimensionality is learning in a reduced-order space using Principal Component Analysis (PCA) (Jolliffe & Cadima, 2016), similar to Kingma et al. (2014), who applied PCA when training VAEs. To address prior-posterior mismatch, future work could explore incorporating domain knowledge to shape the prior’s energy functions and align them with the posterior before training begins, or develop methods for selecting appropriate initial domains and adapting them dynamically.

Additionally, KAEM could learn domain-specific priors that transfer across generator architectures. In this setting, IS may serve as an efficient strategy for rapidly retraining new generators using priors already aligned with the posterior.

Improved expressivity The smaller experiment in Appendix H demonstrated that the choice of prior architecture and its encoded inductive biases significantly affect sample quality—the alternative basis achieved superior image metrics after only 16,000 parameter updates. Future work could further investigate this phenomenon across different KAN bases and datasets, as well as explore how domain knowledge can guide the selection of univariate functions.

Additionally, it is often desirable to enrich the latent space with more expressive distributions. For example, Normalizing Flows (Papamakarios et al., 2021) apply a sequence of reversible transformations that progressively map a simple base distribution into a complex one. This might be achievable in KAEM by introducing more latent distributions, or revising Eq. 17 into a Mixture of Experts framework (Cai et al., 2024) where $\alpha_{q,p}$ could be realized as a more flexible kernel to enable different inductive biases.

References

- Annis, J., Evans, N. J., Miller, B. J., and Palmeri, T. J. Thermodynamic integration and steppingstone sampling methods for estimating bayes factors: A tutorial. *Journal of Mathematical Psychology*, 89:67–86, April 2019. doi: 10.1016/j.jmp.2019.01.005. URL <https://osf.io/jpnb4>. Epub 2019 Feb 13.
- Bereska, L. and Gavves, E. Mechanistic interpretability for ai safety – a review, 2024. URL <https://arxiv.org/abs/2404.14082>.
- Bińkowski, M., Sutherland, D. J., Arbel, M., and Gretton, A. Demystifying mmd gans, 2021.
- Biron-Lattes, M., Surjanovic, N., Syed, S., Campbell, T., and Bouchard-Côté, A. automala: Locally adaptive metropolis-adjusted langevin algorithm, 2024. URL <https://arxiv.org/abs/2310.16782>.
- Bohra, P., Campos, J., Gupta, H., Aziznejad, S., and Unser, M. Learning activation functions in deep (spline) neural networks. *IEEE Open Journal of Signal Processing*, 1: 295–309, 2020. doi: 10.1109/OJSP.2020.3039379.
- Bozorgasl, Z. and Chen, H. Wav-kan: Wavelet kolmogorov-arnold networks, 2024. URL <https://arxiv.org/abs/2405.12832>.
- Brooks, S., Gelman, A., Jones, G., and Meng, X.-L. *Handbook of Markov Chain Monte Carlo*. Chapman and Hall/CRC, May 2011. ISBN 9780429138508. doi: 10.1201/b10905. URL <http://dx.doi.org/10.1201/b10905>.
- Cai, W., Jiang, J., Wang, F., Tang, J., Kim, S., and Huang, J. A survey on mixture of experts, 2024. URL <https://arxiv.org/abs/2407.06204>.
- Calderhead, B. and Girolami, M. Estimating bayes factors via thermodynamic integration and population mcmc. *Computational Statistics & Data Analysis*, 53(12):4028–4045, 2009. ISSN 0167-9473. doi: <https://doi.org/10.1016/j.csda.2009.07.025>. URL <https://www.sciencedirect.com/science/article/pii/S0167947309002722>.
- Champion, K., Lusch, B., Kutz, J. N., and Brunton, S. L. Data-driven discovery of coordinates and governing equations. *Proceedings of the National Academy of Sciences*, 116(45):22445–22451, October 2019. ISSN 1091-6490. doi: 10.1073/pnas.1906995116. URL <http://dx.doi.org/10.1073/pnas.1906995116>.
- Chong, M. J. and Forsyth, D. Effectively unbiased fid and inception score and where to find them, 2020.
- Cui, J. and Han, T. Learning latent space hierarchical ebm diffusion models, 2024. URL <https://arxiv.org/abs/2405.13910>.
- Deng, L. The mnist database of handwritten digit images for machine learning research. *IEEE Signal Processing Magazine*, 29(6):141–142, 2012.
- Devroye, L. *Non-Uniform Random Variate Generation*. Springer-Verlag, New York, 1986. ISBN 0-387-96305-7.
- Devroye, L. Chapter 4 nonuniform random variate generation. In Henderson, S. G. and Nelson, B. L. (eds.), *Simulation*, volume 13 of *Handbooks in Operations Research and Management Science*, pp. 83–121. Elsevier, 2006. doi: [https://doi.org/10.1016/S0927-0507\(06\)13004-2](https://doi.org/10.1016/S0927-0507(06)13004-2). URL <https://www.sciencedirect.com/science/article/pii/S0927050706130042>.
- Douc, R., Cappé, O., and Moulines, E. Comparison of resampling schemes for particle filtering, 2005. URL <https://arxiv.org/abs/cs/0507025>.

- Dupuis, P. and Wang, H. Importance sampling, large deviations, and differential games. *Stochastics and Stochastic Reports*, 76:481–508, 2004.
- Dzhenezher, S. and Skopenkov, A. A structured proof of kolmogorov’s superposition theorem, 2022. URL <https://arxiv.org/abs/2105.00408>.
- EnzymeAD and Reactant.jl Contributors. Reactant.jl: Optimize julia functions with mlir and xla. <https://github.com/EnzymeAD/Reactant.jl>, 2025. Julia package. Version v0.2.181, accessed 2025-12-07.
- Friel, N. and Pettitt, A. N. Marginal likelihood estimation via power posteriors. *Journal of the Royal Statistical Society. Series B (Statistical Methodology)*, 70(3):589–607, 2008. ISSN 13697412, 14679868. URL <http://www.jstor.org/stable/20203843>.
- Fu, H., Li, C., Liu, X., Gao, J., Celikyilmaz, A., and Carin, L. Cyclical annealing schedule: A simple approach to mitigating kl vanishing, 2019. URL <https://arxiv.org/abs/1903.10145>.
- Givental, A. B., Khesin, B. A., Marsden, J. E., Varchenko, A. N., Vassiliev, V. A., Viro, O. Y., and Zakalyukin, V. M. (eds.). *On the representation of functions of several variables as a superposition of functions of a smaller number of variables*, pp. 25–46. Springer Berlin Heidelberg, Berlin, Heidelberg, 2009. ISBN 978-3-642-01742-1. doi: 10.1007/978-3-642-01742-1_5. URL https://doi.org/10.1007/978-3-642-01742-1_5.
- Goertzel, G. Quota sampling and importance functions in stochastic solution of particle problems. Technical Report AECD-2793, U.S. Atomic Energy Commission, 1949. Technical Report, June 21, 1949.
- Goodfellow, I. J., Pouget-Abadie, J., Mirza, M., Xu, B., Warde-Farley, D., Ozair, S., Courville, A., and Bengio, Y. Generative adversarial networks, 2014. URL <https://arxiv.org/abs/1406.2661>.
- Heusel, M., Ramsauer, H., Unterthiner, T., Nessler, B., and Hochreiter, S. Gans trained by a two time-scale update rule converge to a local nash equilibrium, 2018.
- Hukushima, K. and Nemoto, K. Exchange monte carlo method and application to spin glass simulations. *Journal of the Physical Society of Japan*, 65(6):1604–1608, June 1996. ISSN 1347-4073. doi: 10.1143/jpsj.65.1604. URL <http://dx.doi.org/10.1143/JPSJ.65.1604>.
- Jolliffe, I. T. and Cadima, J. Principal component analysis: a review and recent developments. *Philosophical Transactions of the Royal Society A: Mathematical, Physical and Engineering Sciences*, 374(2065):20150202, 2016. ISSN 1364-503X. doi: 10.1098/rsta.2015.0202.
- JuliaCI. Benchmarktools.jl, 2024. URL <https://juliaci.github.io/BenchmarkTools.jl/stable/>. Accessed on August 20, 2024.
- Karniadakis, G. E., Kevrekidis, I. G., Lu, L., Perdikaris, P., Wang, S., and Yang, L. Physics-informed machine learning. *Nature Reviews Physics*, 3(6):422–440, 2021. ISSN 2522-5820. doi: 10.1038/s42254-021-00314-5. URL <https://doi.org/10.1038/s42254-021-00314-5>.
- Kingma, D. P. and Welling, M. Auto-encoding variational bayes, 2022. URL <https://arxiv.org/abs/1312.6114>. arXiv:1312.6114.
- Kingma, D. P., Rezende, D. J., Mohamed, S., and Welling, M. Semi-supervised learning with deep generative models, 2014. URL <https://arxiv.org/abs/1406.5298>.
- Kloek, T. and van Dijk, H. K. Bayesian estimates of equation system parameters: An application of integration by monte carlo. *Econometrica*, 46(1):1–19, 1978. ISSN 00129682, 14680262. URL <http://www.jstor.org/stable/1913641>.
- Kong, D., Pang, B., and Wu, Y. N. Unsupervised meta-learning via latent space energy-based model of symbol vector coupling. In *Fifth Workshop on Meta-Learning at the Conference on Neural Information Processing Systems*, 2021. URL <https://openreview.net/forum?id=-pLftu7EpXz>.
- Larson, R. and Edwards, B. *Calculus of a Single Variable*. Cengage Learning, 2008. ISBN 9780547209982. URL https://books.google.co.uk/books?id=gR7nGg5_9xcC.
- Lattner, C., Amini, M., Bondhugula, U., Cohen, A., Davis, A., Pienaar, J., Riddle, R., Shpeisman, T., Vasilache, N., and Zinenko, O. Mlir: A compiler infrastructure for the end of moore’s law, 2020. URL <https://arxiv.org/abs/2002.11054>.
- Laurie, D. Calculation of gauss-kronrod quadrature rules. *Math. Comput.*, 66:1133–1145, 07 1997. doi: 10.1090/S0025-5718-97-00861-2.
- LeCun, Y., Bengio, Y., and Hinton, G. Deep learning. *Nature*, 521(7553):436–444, May 28 2015. ISSN 1476-4687. doi: 10.1038/nature14539.
- Li, Z. Kolmogorov-arnold networks are radial basis function networks, 2024. URL <https://arxiv.org/abs/2405.06721>.
- Liu, Z., Luo, P., Wang, X., and Tang, X. Deep learning face attributes in the wild, 2015. URL <https://arxiv.org/abs/1411.7766>.

- Liu, Z., Wang, Y., Vaidya, S., Ruehle, F., Halverson, J., Soljačić, M., Hou, T. Y., and Tegmark, M. Kan: Kolmogorov-arnold networks, 2024. URL <https://arxiv.org/abs/2404.19756>.
- Marinari, E. and Parisi, G. Simulated tempering: A new monte carlo scheme. *Europhysics Letters*, 19(6):451, jul 1992. doi: 10.1209/0295-5075/19/6/002. URL <https://dx.doi.org/10.1209/0295-5075/19/6/002>.
- Metropolis, N. and Ulam, S. The monte carlo method. *Journal of the American Statistical Association*, 44(247): 335–341, 1949. ISSN 01621459, 1537274X. URL <http://www.jstor.org/stable/2280232>.
- Moses, W. and Churavy, V. Instead of rewriting foreign code for machine learning, automatically synthesize fast gradients. In *Advances in Neural Information Processing Systems*, volume 33, pp. 12472–12485. Curran Associates, Inc., 2020.
- Moses, W. S., Churavy, V., Paehler, L., Hüchelheim, J., Narayanan, S. H. K., Schanen, M., and Doerfert, J. Reverse-mode automatic differentiation and optimization of gpu kernels via enzyme. In *Proceedings of the International Conference for High Performance Computing, Networking, Storage and Analysis*. Association for Computing Machinery, 2021.
- Moses, W. S., Narayanan, S. H. K., Paehler, L., Churavy, V., Schanen, M., Hüchelheim, J., Doerfert, J., and Holland, P. Scalable automatic differentiation of multiple parallel paradigms through compiler augmentation. In *Proceedings of the International Conference on High Performance Computing, Networking, Storage and Analysis*. IEEE Press, 2022.
- Neal, R. M. Annealed importance sampling, 1998. URL <https://arxiv.org/abs/physics/9803008>.
- Netzer, Y., Wang, T., Coates, A., Bissacco, A., Wu, B., and Ng, A. Y. Reading digits in natural images with unsupervised feature learning. In *NIPS Workshop on Deep Learning and Unsupervised Feature Learning 2011*, 2011. URL http://ufldl.stanford.edu/housenumbers/nips2011_housenumbers.pdf.
- Nijkamp, E., Hill, M., Han, T., Zhu, S.-C., and Wu, Y. N. On the anatomy of mcmc-based maximum likelihood learning of energy-based models, 2019a. URL <https://arxiv.org/abs/1903.12370>.
- Nijkamp, E., Hill, M., Zhu, S.-C., and Wu, Y. N. Learning non-convergent non-persistent short-run mcmc toward energy-based model, 2019b. URL <https://arxiv.org/abs/1904.09770>.
- Pang, B., Han, T., Nijkamp, E., Zhu, S.-C., and Wu, Y. N. Learning latent space energy-based prior model, 2020. URL <https://arxiv.org/abs/2006.08205>.
- Papamakarios, G., Nalisnick, E., Rezende, D. J., Mohamed, S., and Lakshminarayanan, B. Normalizing flows for probabilistic modeling and inference, 2021. URL <https://arxiv.org/abs/1912.02762>.
- Poggio, T. and Girosi, F. Networks for approximation and learning. *Proceedings of the IEEE*, 78(9):1481–1497, 1990. doi: 10.1109/5.58326. URL <https://doi.org/10.1109/5.58326>.
- Rivera, M. How to train your vae, 2024. URL <https://arxiv.org/abs/2309.13160>.
- Roberts, G. O. and Stramer, O. Langevin diffusions and metropolis-hastings algorithms. *Methodology and Computing in Applied Probability*, 4(4): 337–357, 2002. ISSN 1573-7713. doi: 10.1023/A:1023562417138. URL <https://doi.org/10.1023/A:1023562417138>.
- Rosicky, P. J., Doll, J. D., and Friedman, H. L. Brownian dynamics as smart monte carlo simulation. *The Journal of Chemical Physics*, 69(10):4628–4633, 1978. doi: 10.1063/1.436415.
- Swendsen, R. and Wang, J.-S. Replica monte carlo simulation of spin-glasses. *Physical review letters*, 57:2607–2609, 12 1986. doi: 10.1103/PhysRevLett.57.2607.
- Szegedy, C., Vanhoucke, V., Ioffe, S., Shlens, J., and Wojna, Z. Rethinking the inception architecture for computer vision, 2015.
- Xiao, H., Rasul, K., and Vollgraf, R. Fashion-mnist: a novel image dataset for benchmarking machine learning algorithms, 2017. URL <https://arxiv.org/abs/1708.07747>.
- Zettascale Computing Corporation. Zettascale: Energy efficient reconfigurable dataflow chips for ai. <https://zsc.ai>, 2026. Accessed: 2026-01-30. Based in Silicon Valley, building energy-efficient reconfigurable AI chips (“XPU”) and backed by Y Combinator.
- Zhang, X., Tan, Z., and Ou, Z. Persistently trained, diffusion-assisted energy-based models, 2023. URL <https://arxiv.org/abs/2304.10707>.

A. Benchmarks

Benchmarks were collected for KAEM and the VAE baseline in FP32 on an NVIDIA GeForce RTX 4060 GPU using Julia’s BenchmarkTools package (JuliaCI, 2024). Compilation and reverse differentiation were performed using Julia’s Reactant (EnzymeAD & Reactant.jl Contributors, 2025) and Enzyme (Moses & Churavy, 2020; Moses et al., 2021; 2022) packages. All benchmarks are based on the hyperparameters and architectures used for SVHN (32×32), and reflect a reverse autodifferentiation of the training criteria in Eqs. 4 and 24, or the prior sampling process during inference. Note that garbage collection (GC) is zero in all cases, as Reactant compiles away all intermediate allocations.

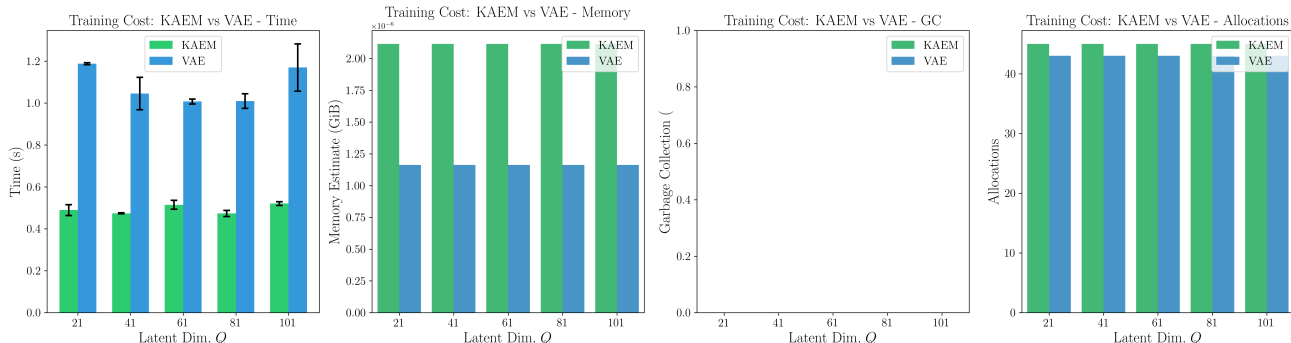


Figure 5. Training cost comparison (single training step) between KAEM (MLE with importance sampling) and VAE across latent dimensions $Q \in \{21, 41, 61, 81, 101\}$. Metrics shown include execution time (with error bars), memory usage, garbage collection percentage, and allocations.

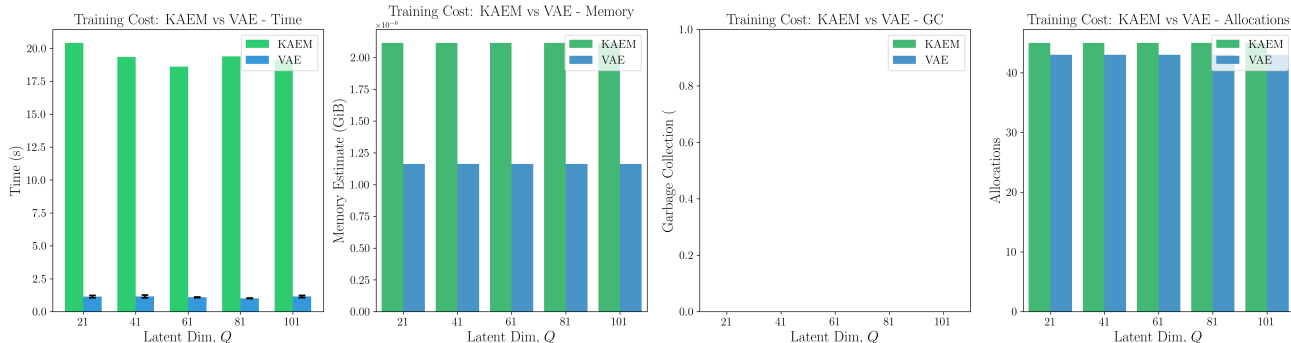


Figure 6. Training cost comparison (single training step) between KAEM (MLE with 40 ULA iterations) and VAE across latent dimensions $Q \in \{21, 41, 61, 81, 101\}$. Metrics shown include execution time (with error bars), memory usage, garbage collection percentage, and allocations.

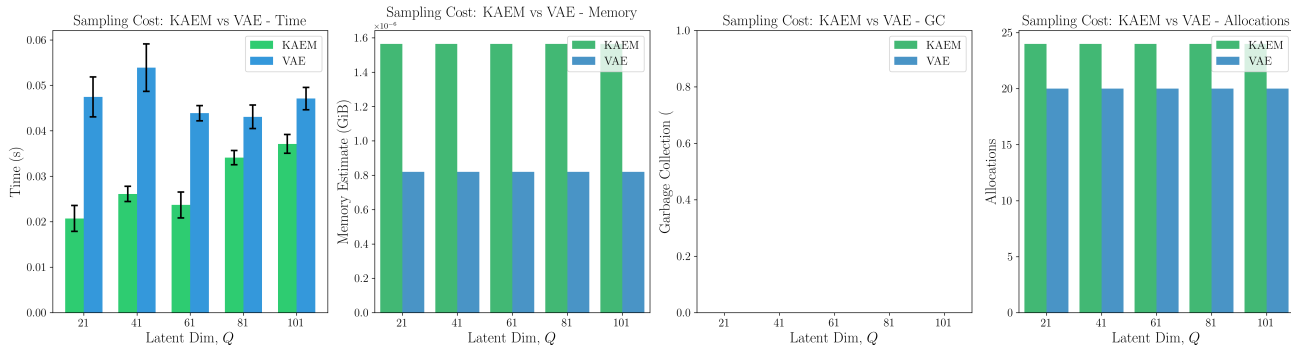


Figure 7. Sampling cost comparison between KAEM (MLE) and VAE across latent dimensions. KAEM uses inverse transform sampling (ITS) from the EBM prior, while VAE decodes from $z \sim \mathcal{N}(\mathbf{0}, \mathbf{I})$.

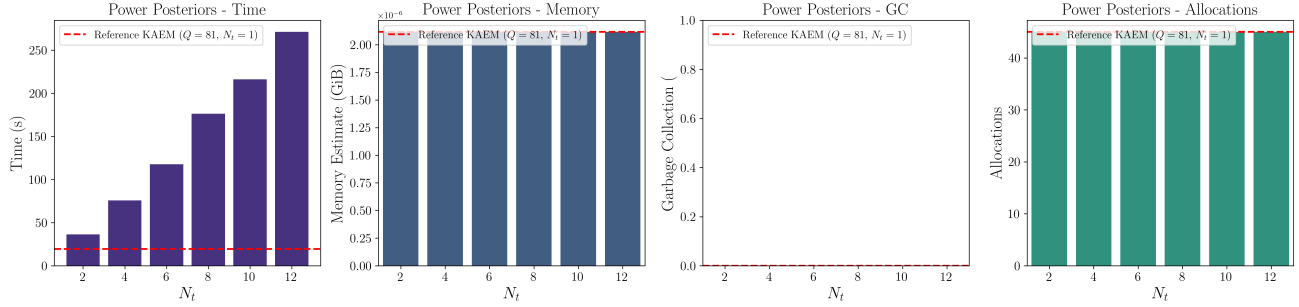


Figure 8. KAEM thermodynamic training cost scaling with the number of power posteriors $N_t \in \{2, 4, 6, 8, 10, 12\}$. The red dashed line indicates the reference cost at $Q = 81$ with $N_t = 1$ (single posterior, no thermodynamic integration), demonstrating the computational overhead of using multiple temperature replicas.

B. Interpreting the Kolmogorov-Arnold theorem

B.1. Inner functions as Markov kernels

In Eq. 13, $F_{\pi_{q,p}}^{-1} : [0, 1] \rightarrow \mathcal{Z}$ is the generalized inverse CDF associated with a parameterized latent measure, $\pi_{q,p}$ in the latent space, $\mathcal{Z} \subset \mathbb{R}$. We have therefore interpreted $u_p \sim \text{Unif}(0, 1)$ in Eq. 1 as a uniform random variable in the probability space, $([0, 1], \mathcal{B}([0, 1]), \mu)$, where $\mathcal{B}([0, 1])$ is the Borel σ -algebra on $[0, 1]$ and μ is the uniform probability measure on $[0, 1]$. This is valid under standard regularity assumptions on F , since it is a measurable, monotone, increasing function, and thus $F_{\pi_{q,p}}^{-1}(u) = \inf \{z \in \mathcal{Z} : F_{\pi_{q,p}}(z) \geq u\}$ is a measurable pushforward (Markov kernel) between the probability spaces:

$$([0, 1], \mathcal{B}([0, 1]), \mu) \xrightarrow{F_{\pi_{q,p}}^{-1}} (\mathcal{Z}, \mathcal{B}(\mathcal{Z}), \pi_{q,p}), \quad (26)$$

Under exponential tilting, the latent measure $\pi_{q,p}$ against a base measure π_0 can therefore be viewed from the lens of the Radon–Nikodym derivative:

$$d\pi_{q,p}(z) = \frac{\exp(f_{q,p}(z))}{Z_{q,p}} d\pi_0(z), \quad (27)$$

where $f_{q,p}(z)$ is our learned energy function and $Z_{q,p}$ is the finite normalizing constant (partition function) that ensures $\pi_{q,p}$ induces a valid probability density, $p_{q,p}$, for each latent feature. The inspiration for this exponential tilting form can be traced to the energy-based prior introduced by Pang et al. (2020), adapted to the univariate case. The base prior π_0 serves as a reference that guides the form of the learned $\pi_{q,p}$, allowing for flexible reweighting via the energy function $f_{q,p}$. For $\pi_{q,p}$ to define a valid density, which we denote $p_{q,p}$, we require exponential Lebesgue-integrability:

$$\begin{aligned} \exp(f_{q,p}(z)) &\in L^1(\pi_0) \\ \text{such that } Z_{q,p} &= \int_{\mathcal{Z}} \exp(f_{q,p}(z)) \pi_0(dz) < \infty. \end{aligned} \quad (28)$$

As a result, the model retains a coherent probabilistic interpretation of Eq. 1 that is consistent with the energy-based framework proposed by Pang et al. (2020), which is well suited to maximum likelihood training.

B.2. Kolmogorov-Arnold Network generator

Having sampled the intermediary latent variable with ITS such that $z_{q,p} = F_{\pi_{q,p}}^{-1}(u_p)$, the generator can be realized as:

$$\tilde{\mathbf{x}} = G_{\Phi}(\mathbf{z}) + \boldsymbol{\varepsilon}, \quad \text{where } \mathbf{z} \sim p_f(\mathbf{z}), \quad \boldsymbol{\varepsilon} \sim \mathcal{N}(\mathbf{0}, \sigma_{\text{noise}} \mathbf{I}), \quad (29)$$

where $\tilde{\mathbf{x}} = \{\tilde{x}_o\}_{o=1}^{n_x}$ represents a generated data sample and n_x is used to specify the dimension of $\tilde{\mathbf{x}}$. The architecture may be made strictly adherent to KART using a Kolmogorov-Arnold Network (KAN):

$$\tilde{x}_o = \sum_{q=1}^{2n_z+1} \Phi_{o,q} \left(\sum_{p=1}^{n_z} z_{q,p} \right) + \varepsilon_o, \quad \tilde{\mathbf{x}} = \begin{pmatrix} \sum_{q=1}^{2n_z+1} \Phi_{1,q} \left(\sum_{p=1}^{n_z} z_{q,p} \right) \\ \sum_{q=1}^{2n_z+1} \Phi_{2,q} \left(\sum_{p=1}^{n_z} z_{q,p} \right) \\ \vdots \\ \sum_{q=1}^{2n_z+1} \Phi_{n_x,q} \left(\sum_{p=1}^{n_z} z_{q,p} \right) \end{pmatrix} + \boldsymbol{\varepsilon}. \quad (30)$$

The functions, $\Phi_{o,q} : \mathbb{R} \rightarrow \mathbb{R}$, are realizable as basis or KAN functions similar to $f_{q,p} : \mathcal{Z} \rightarrow \mathbb{R}$.

Deepening this generator, as guided by Liu et al. (2024) for KANs, does not replace KART as the inner foundation of KAEM:

$$x_o = \sum_{l_n=1}^{L_n} h_{o,l_n} \left(\dots h_{l_3,l_2} \left(\sum_{l_1=1}^{L_1} h_{l_2,l_1} \left(\sum_{q=1}^{2n_z+1} \Phi_{l_1,q} \left(\sum_{p=1}^{n_z} z_{q,p} \right) \right) \right) \right) + \varepsilon_o. \quad (31)$$

Here, each h represents a hidden layer introduced between the outer sum of Eq. 1, and the output feature space to allow for more expressivity when required. In fact, each successive instance of h can be interpreted as a distinct outer sum of Eq. 1, where the inner sum corresponds to the previous layer. This is valid provided that:

$$L_1 = 2(2n_z + 1) + 1, \quad L_2 = 2L_1 + 1, \quad \dots \quad L_n = 2L_{n-1} + 1. \quad (32)$$

Thus, a smooth transition between the latent and data space can be achieved by progressively doubling widths, eliminating the need for arbitrary choices while maintaining compliance with KART. Strict adherence to KART can be achieved for hidden layer $h_{l_k,l_{k-1}}$ by applying either a sigmoid or affine transformation after layer $h_{l_{k-2},l_{k-3}}$ to shift its range back to $[0, 1]^{L_{k-1}}$. However, using sigmoid may lead to vanishing gradients and we suggest that function domains are less critical to KART than its structural bias and should not be prioritized over maintaining gradient flow and avoiding saturation.

C. Importance sampling

C.1. Theory

Importance Sampling (IS) is a Monte Carlo that enables the estimation of expectations with respect to one probability measure using samples drawn from another. For a detailed exposition, see Kloek & van Dijk (1978).

The Radon-Nikodym derivative IS involves rewriting the expectation of an arbitrary function or density, $\rho(\mathbf{z})$, under the target measure, $\mathbb{P}(\mathbf{z})$, in terms of a more tractable proposal measure, $\mathbb{Q}(\mathbf{z})$. Specifically, we use the Radon-Nikodym derivative $\frac{d\mathbb{P}}{d\mathbb{Q}}$ to rewrite the expectation of an arbitrary function of \mathbf{z} , denoted as $\rho(\mathbf{z})$:

$$\mathbb{E}_{\mathbb{P}}[\rho(\mathbf{z})] = \int_{\bar{\mathcal{Z}}} \rho(\mathbf{z}) \mathbb{P}(d\mathbf{z}) = \int_{\bar{\mathcal{Z}}} \rho(\mathbf{z}) \cdot \frac{d\mathbb{P}}{d\mathbb{Q}} \mathbb{Q}(d\mathbf{z}). \quad (33)$$

Here, $\frac{d\mathbb{P}}{d\mathbb{Q}}$ acts as a weight that adjusts the contribution of each sample to account for the difference between the target and proposal measures. This requires that the proposal measure \mathbb{Q} is absolutely continuous with respect to the target measure \mathbb{P} , i.e. $\mathbb{Q}(A) = 0$ implies $\mathbb{P}(A) = 0$, for every measurable subset $A \in \mathcal{Z}$.

In the context of KAEM, the target density is the posterior, $p_{f,\Phi}(\mathbf{z} | \mathbf{x})$, which is proportional to the product of the likelihood and the prior:

$$p_{f,\Phi}(\mathbf{z} | \mathbf{x}) \propto p_{\Phi}(\mathbf{x} | \mathbf{z}) \cdot p_f(\mathbf{z}). \quad (34)$$

The exact normalization constant, (the marginal likelihood $p_{f,\Phi}(\mathbf{x})$), is intractable, but IS circumvents the need to compute it explicitly. Instead, the expectation of $\rho(\mathbf{z})$ under the posterior can be expressed as:

$$\mathbb{E}_{p_{f,\Phi}(\mathbf{z}|\mathbf{x})}[\rho(\mathbf{z})] = \int_{\bar{\mathcal{Z}}} \rho(\mathbf{z}) w(\mathbf{z}) q(\mathbf{z}) d\mathbf{z}, \quad (35)$$

where the importance weights $w(\mathbf{z})$ are given by:

$$w(\mathbf{z}) = \frac{p_{f,\Phi}(\mathbf{z} | \mathbf{x})}{q(\mathbf{z})} = \frac{p_{\Phi}(\mathbf{x} | \mathbf{z}) \cdot p_f(\mathbf{z})}{q(\mathbf{z})}. \quad (36)$$

Proposal distribution and importance weights A practical choice for the proposal density $q(\mathbf{z})$ is the prior, $p_f(\mathbf{z})$, given the availability of draws from the prior using the method outlined in Algorithm 1. This simplifies the importance weights, as the prior has a tractable form and covers the support of the posterior. This yields:

$$w(\mathbf{z}^{(s)}) = p_{\Phi}(\mathbf{x} | \mathbf{z}^{(s)}) \propto \exp(\log(p_{\Phi}(\mathbf{x} | \mathbf{z}^{(s)}))). \quad (37)$$

This reflects that the likelihood now directly informs how much weight to assign to each sample \mathbf{z} . Intuitively, samples that better explain the observed data \mathbf{x} , (as measured by the likelihood), are given higher importance. Using the definition of softmax, the normalized weights are given by:

$$\frac{w(\mathbf{z}^{(s)})}{\sum_{r=1}^N w(\mathbf{z}^{(r)})} = \text{softmax}_s \left(\log(p_{\Phi}(\mathbf{x} | \mathbf{z}^{(s)})) \right). \quad (38)$$

Resampling The suitability of these weights depends on how well $q(\mathbf{z})$ matches the posterior. In KAEM, there is likely to be significant mismatch due to the complexity of the likelihood used in Eq. 8. Consequently, the weights will exhibit high variance, resulting in many samples contributing minimally. This reduces the Effective Sample Size (ESS) and introduces bias into the estimates.

To address this, the weights are resampled before proceeding with the posterior expectation. This is accomplished by using one of the methods outlined by Douc et al. (2005), whenever the ESS falls below a certain threshold determined by $\text{ESS} < \gamma * N$, where γ is a hyperparameter controlling resample rate and N is the number of samples. Resampling redistributes the sample weights, creating a new population with uniformly distributed weights while preserving the statistical properties of the original distribution. As training progresses and the prior becomes a better match for the posterior, the need for resampling decreases.

After resampling, the corresponding weights will be uniformly distributed and a standard Monte Carlo estimator can be applied instead of the IS estimator.

Importance Sampling estimator To estimate the expectation, we draw N independent samples $\{\mathbf{z}^{(s)}\}_{s=1}^N \sim q(\mathbf{z}) = p_f(\mathbf{z})$ using the procedure outlined in Algorithm 1 and compute a weighted sum:

$$\mathbb{E}_{p_{f,\Phi}(\mathbf{z}|\mathbf{x})}[\rho(\mathbf{z})] \approx \sum_{s=1}^N \rho(\mathbf{z}^{(s)}) \cdot w_{\text{norm}}(\mathbf{z}^{(s)}) \approx \frac{1}{N} \sum_{s=1}^N \rho(\mathbf{z}_{\text{resampled}}^{(s)}). \quad (39)$$

The estimator is unbiased, implying that its expectation matches the true posterior expectation. As $N \rightarrow \infty$, the approximation converges almost surely to the true value, provided that $q(\mathbf{z})$ sufficiently covers the posterior to ensure a well-conditioned Radon-Nikodym derivative. This estimator is used for the log-marginal likelihood and its gradient in Eqs. 4, since it provides a means of estimating expectations with respect to the posterior.

C.2. Residual resampling

In this study, we adopted residual resampling to filter the population of latent samples whenever the effective sample size (ESS) criterion in Algorithm 2 is satisfied. Given a set of normalized weights $\{w_{\text{norm}}(\mathbf{z}^{(s)})\}_{s=1}^N$, the method deterministically replicates samples according to the integer part of Nw_{norm} , and uses multinomial sampling to allocate the remaining draws according to the residual mass.

D. Guidance on annealing

D.1. Cyclic annealing

Given the form of Eq. 12, setting $t = 0$ results in the power posterior density assuming the form of the prior. As t increments, the power posterior gradually adopts a shape more closely resembling the true Bayesian posterior. At $t = 1$, the power posterior converges fully on the original posterior.

The effect of tempering is illustrated in Fig. 9, starting with a Gaussian prior that is entirely uninformed of \boldsymbol{x} . As t increases from 0 to 1, the contribution of the likelihood term in Eq. 12 progressively grows, ultimately leading to the posterior at $t = 1$. This final posterior can be interpreted as the prior updated by information from the samples of \boldsymbol{x} .

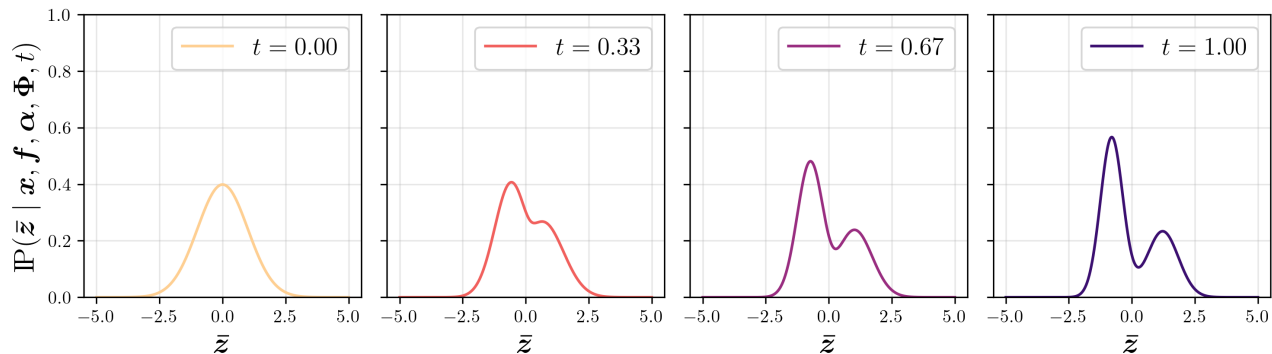


Figure 9. Demonstration of power posterior evolution with t . A simple Gaussian prior is sculpted into forms that resemble a more complex, multi-modal posterior as t is incremented from 0 to 1.

Calderhead & Girolami (2009) demonstrated that uniformly scheduling the discretized temperatures in Eq. 22 results in unequal contributions of adjacent power posteriors to the Thermodynamic Integral. The success of TI and SE, relies on selecting each t_k to ensure sufficient overlap of adjacent power posteriors. This overlap ensures similarity between adjacent power posteriors, as introduced in Sec. C.1, which influences the Monte Carlo estimator in Eq. 24, given that SE is an application of importance sampling, (Annis et al., 2019).

This overlap is quantified by the KL divergence term in Eq. 55. Maintaining small KL divergences between adjacent power posteriors can be achieved by clustering temperatures in regions where $p_{f,\Phi}(z | \boldsymbol{x}, t_k)$ changes rapidly. To accomplish this, we follow Calderhead & Girolami (2009) in adopting a power-law relationship to schedule the temperatures of Eq. 22:

$$t_k = \left(\frac{k}{N_t} \right)^p, \quad k = 0, 1, \dots, N_t, \quad (40)$$

The effect of varying p on the schedule between 0 and 1 is visualized in Fig. 10. When $p > 1$, spacing becomes denser near $t = 0$, while $p < 1$ creates denser spacing near $t = 1$. The impact of varying p on the discretized Thermodynamic Integral of Eq. 55 is illustrated in Fig. 11. The plots demonstrate that for $p > 1$, the trapezoidal bins are clustered closer to $t = 0$, concentrating the discrete approximation error towards $t = 1$.

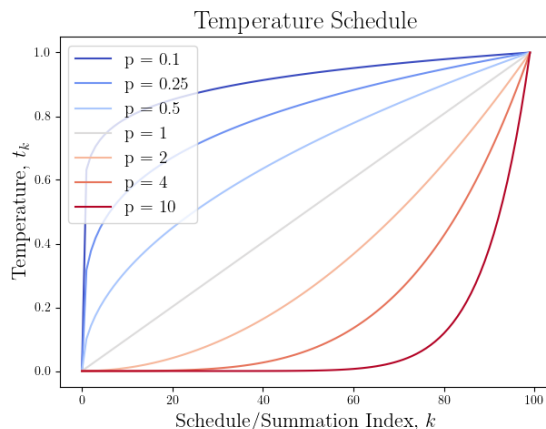
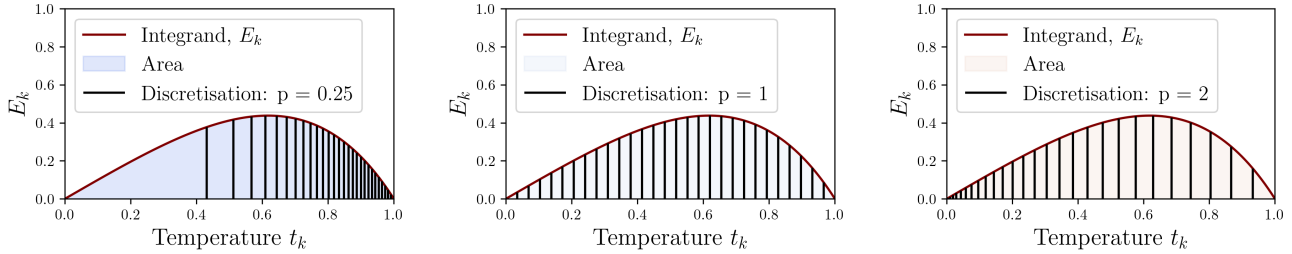


Figure 10. Power-law schedule.



(a) $p = 0.25$ schedule has more bins clustered towards $t = 1$. (b) $p = 1$ schedule is uniformly distributed between the bounds. (c) $p = 2$ schedule has more bins clustered towards $t = 0$.

Figure 11. Effect of power-law schedule clusters on integral approximation error. Evaluation points can be skewed towards a particular bound by choosing p . Increasing p provides more tempering, concentrating more evaluation points on smoother likelihoods. Tempering helps to mitigate practical challenges associated with the non-smoothness of the univariate functions in Eq. 1.

The study by [Calderhead & Girolami \(2009\)](#) derives an analytic term for an optimal tempering distribution in the context of linear regression models, where the power posterior in Eq. 12 is used to evaluate the plausibility of model parameters in relation to the data, rather than reflecting a latent variable posterior. However, their findings may not hold in the context of KAEM and generative modeling, making p and the temperature schedule difficult variables to tune.

Instead, we schedule p sinusoidally across all training parameter updates, starting with a lower value of p and ending with a higher value, treated as tunable hyperparameters.

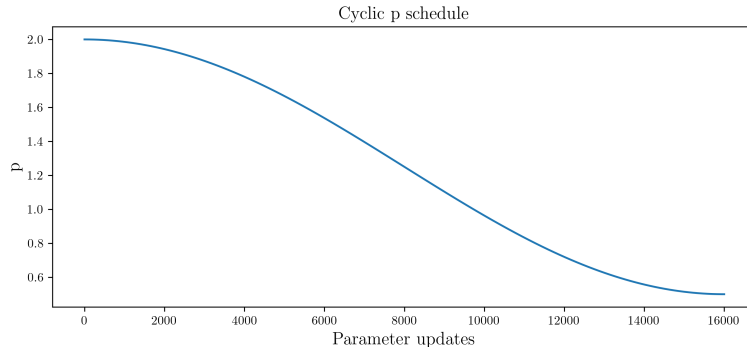


Figure 12. Cosine p schedule, decreasing from 2 to 0.5

Initializing $p > 1$ focuses learning on low-variance, smoother power posteriors during the early stages of the cycle, where global features emerge between adjacent power posteriors. As training progresses, KAEM will have learned the global features sufficiently well, reducing the change of density between adjacent power posteriors of a $p > 1$ schedule. At this stage, $p(i)$ will have transitioned to $p \leq 1$, thereby shifting KAEM’s focus towards capturing more high-variance, data-informed features of the posterior landscape, where training is expected to enhance its ability to generate finer details.

Guidance on selecting optimal values for the tempering hyperparameters is provided in Tab. 3.

D.2. Choosing hyperparameters

Table 3. Tempering hyperparameters.

Hyperparameter	Description
$N_t > 1$	Specifies the number of power posteriors, enabling a smooth transition between the prior and posterior. Increasing this improves exploration but also increases cost due to the need for more MALA iterations. Typically, this is memory-bound and guided by hardware availability, such as $N_t = 5$.
$N_{\text{local}} > 1$	Determines the number of ULA or autoMALA iterations per power posterior. Although increasing this value improves the quality of samples at each stage, it also raises the computational cost, much like N_t . It can be kept at a small value, such as $N_{\text{local}} = 40$, (based on the recommendations of Nijkamp et al. (2019b;a) regarding short-run Markov chain Monte Carlo).
$p_{\text{init}} > 1$, $p_{\text{end}} \leq 1$, $N_{\text{cycles}} \geq 0$	Controls the evolution of tempering during training. If the data is expected to have smooth relationships, reduce both p_{init} and p_{end} . For data with finer details, increase both values to allow for better focus on capturing intricate features. The values used for this study were $p_{\text{init}} = 3$, and $p_{\text{end}} = 1$, since our experience suggests that power posteriors initially change rapidly closer to the prior. The number of cycles, N_{cycles} , controls the periodicity of cosine scheduling similar to cyclic annealing (Fu et al., 2019).

E. Derivations and useful identities

E.0.1. USEFUL PROOF

The following short proof for a learning gradient with respect to an arbitrary set of parameters, θ , proves useful for other derivations in this study:

$$\begin{aligned}
 \mathbb{E}_{p_{\theta}(\mathbf{x})} [\nabla_{\theta} \log p_{\theta}(\mathbf{x})] &= \mathbb{E}_{p_{\theta}(\mathbf{x})} \left[\frac{\nabla_{\theta} p_{\theta}(\mathbf{x})}{p_{\theta}(\mathbf{x})} \right] = \int_{\mathcal{X}} \frac{\nabla_{\theta} p_{\theta}(\mathbf{x})}{p_{\theta}(\mathbf{x})} p_{\theta}(\mathbf{x}) d\mathbf{x} \\
 &= \int_{\mathcal{X}} \nabla_{\theta} p_{\theta}(\mathbf{x}) d\mathbf{x} = \nabla_{\theta} \int_{\mathcal{X}} p_{\theta}(\mathbf{x}) d\mathbf{x} = \nabla_{\theta} 1 = 0.
 \end{aligned} \tag{41}$$

E.0.2. MARGINAL LIKELIHOOD

$$\begin{aligned}
 \log(p_{f,\Phi}(\mathbf{x})) &= \mathbb{E}_{p_{f,\Phi}(\mathbf{z}|\mathbf{x})} [\log(p_{f,\Phi}(\mathbf{x}, \mathbf{z}))] \\
 &= \mathbb{E}_{p_{f,\Phi}(\mathbf{z}|\mathbf{x})} [\log(p_f(\mathbf{z}) \cdot p_{\Phi}(\mathbf{x} | \mathbf{z}))] \\
 &= \mathbb{E}_{p_{f,\Phi}(\mathbf{z}|\mathbf{x})} [\log(p_f(\mathbf{z})) + \log(p_{\Phi}(\mathbf{x} | \mathbf{z}))].
 \end{aligned} \tag{42}$$

E.0.3. MAXIMUM LIKELIHOOD LEARNING GRADIENT

This proof demonstrates that the learning gradient with respect to an arbitrary set of parameters, θ , is independent of sampling:

$$\begin{aligned}
 \mathbb{E}_{p(\mathbf{z}|\mathbf{x})} [\nabla_{\theta} \log p(\mathbf{x}, \mathbf{z})] &= \mathbb{E}_{p(\mathbf{z}|\mathbf{x})} [\nabla_{\theta} \log p(\mathbf{z} | \mathbf{x}) + \nabla_{\theta} \log p(\mathbf{x})] \\
 &= \mathbb{E}_{p(\mathbf{z}|\mathbf{x})} [\nabla_{\theta} \log p(\mathbf{z} | \mathbf{x})] + \mathbb{E}_{p(\mathbf{z}|\mathbf{x})} [\nabla_{\theta} \log p(\mathbf{x})] \\
 &= 0 + \nabla_{\theta} \log p(\mathbf{x}),
 \end{aligned} \tag{43}$$

where Eq. 41 has been used to zero the expected posterior. This allows gradient flow to be disregarded in sampling procedures as shown in Eq. 4.

E.0.4. CONTRASTIVE DIVERGENCE LEARNING GRADIENT FOR UNIVARIATE LOG-PRIOR

The learning gradient attributed to the univariate KAEM prior in Eq. 14 can be derived into a contrastive divergence framework, which is more typical of energy-based modeling literature. The prior model is solely dependent on f in Eq. 14. We can rewrite Eq. 15 as:

$$\nabla_f \log(p_f(\mathbf{z})) = \nabla_f \sum_{q=1}^{2n_z+1} \sum_{p=1}^{n_z} \log(p_{q,p}(z)) = \nabla_f \sum_{q=1}^{2n_z+1} \sum_{p=1}^{n_z} f_{q,p}(z) + \log(\pi_0(z)) - \log Z_{q,p} \quad (44)$$

where $z = \int_{\mathcal{Z}} \exp(f_{q,p}(z_p)) d\pi_0(z_p)$ is the normalization constant. We can simplify the constant using Eq. 41:

$$\begin{aligned} \mathbb{E}_{p_f(\mathbf{z})} \left[\nabla_f \log p_f(\mathbf{z}) \right] &= \mathbb{E}_{p_f(\mathbf{z})} \left[\nabla_f \sum_{q=1}^{2n_z+1} \sum_{p=1}^{n_z} f_{q,p}(z) + \log(\pi_0(z)) - \log Z_{q,p} \right] = 0 \\ &= \mathbb{E}_{p_f(\mathbf{z})} \left[\nabla_f \sum_{q=1}^{2n_z+1} \sum_{p=1}^{n_z} f_{q,p}(z) \right] - \nabla_f \sum_{q=1}^{2n_z+1} \sum_{p=1}^{n_z} \log Z_{q,p} = 0 \\ \therefore \nabla_f \sum_{q=1}^{2n_z+1} \sum_{p=1}^{n_z} \log Z_{q,p} &= \mathbb{E}_{p_f(\mathbf{z})} \left[\nabla_f \sum_{q=1}^{2n_z+1} \sum_{p=1}^{n_z} f_{q,p}(z) \right] \end{aligned} \quad (45)$$

Therefore the log-prior gradient of Eq. 44 can be evaluated without quadrature normalization as:

$$\nabla_f \log p_f(\mathbf{z}) = \nabla_f \sum_{q=1}^{2n_z+1} \sum_{p=1}^{n_z} f_{q,p}(z) - \mathbb{E}_{p_f(\mathbf{z})} \left[\nabla_f \sum_{q=1}^{2n_z+1} \sum_{p=1}^{n_z} f_{q,p}(z) \right], \quad (46)$$

and the learning gradient attributed to the prior is finalized into a contrastive divergence format:

$$\begin{aligned} \mathbb{E}_{p_{f,\Phi}(\mathbf{z}|\mathbf{x})} \left[\nabla_f [\log p_f(\mathbf{z})] \right] &= \mathbb{E}_{p_{f,\Phi}(\mathbf{z}|\mathbf{x})} \left[\nabla_f \sum_{q=1}^{2n_z+1} \sum_{p=1}^{n_z} f_{q,p}(z) \right] \\ &\quad - \mathbb{E}_{p_f(\mathbf{z})} \left[\nabla_f \sum_{q=1}^{2n_z+1} \sum_{p=1}^{n_z} f_{q,p}(z) \right]. \end{aligned} \quad (47)$$

E.0.5. DERIVING THE THERMODYNAMIC INTEGRAL

Starting from the power posterior:

$$p_{f,\Phi}(\mathbf{z} | \mathbf{x}, t) = \frac{p_{\Phi}(\mathbf{x} | \mathbf{z})^t p_f(\mathbf{z})}{Z_t} \quad (48)$$

The partition function Z_t is given by:

$$Z_t = \mathbb{E}_{p_f(\mathbf{z})} \left[p_{\Phi}(\mathbf{x} | \mathbf{z})^t \right] \quad (49)$$

Now, differentiating the log-partition function with respect to t :

$$\begin{aligned} \frac{\partial}{\partial t} \log(Z_t) &= \frac{1}{Z_t} \frac{\partial}{\partial t} Z_t = \frac{1}{Z_t} \mathbb{E}_{p_f(\mathbf{z})} \left[\frac{\partial}{\partial t} p_{\Phi}(\mathbf{x} | \mathbf{z})^t \right] \\ &= \frac{1}{Z_t} \mathbb{E}_{p_f(\mathbf{z})} \left[\log p_{\Phi}(\mathbf{x} | \mathbf{z}) \cdot p_{\Phi}(\mathbf{x} | \mathbf{z})^t \right] \\ &= \mathbb{E}_{p_{f,\Phi}(\mathbf{z}|\mathbf{x},t)} [\log p_{\Phi}(\mathbf{x} | \mathbf{z})] \end{aligned} \quad (50)$$

Integrating both sides from 0 to 1:

$$\int_0^1 \frac{\partial}{\partial t} \log(Z_t) dt = \int_0^1 \mathbb{E}_{p_{f,\Phi}(\mathbf{z}|\mathbf{x},t)} [\log p_{\Phi}(\mathbf{x} | \mathbf{z})] dt \quad (51)$$

Using the fundamental theorem of calculus, (Larson & Edwards, 2008):

$$\int_0^1 \frac{\partial}{\partial t} \log(Z_t) dt = \log(Z_{t=1}) - \log(Z_{t=0}) = \int_0^1 \mathbb{E}_{p_{f,\Phi}(\mathbf{z}|\mathbf{x},t)} [\log p_{\Phi}(\mathbf{x} | \mathbf{z})] dt \quad (52)$$

The limits of the integrals can be expressed as:

$$\begin{aligned} \log(Z_{t=0}) &= \log\left(\mathbb{E}_{p_f(\mathbf{z})} [p_{\Phi}(\mathbf{x} | \mathbf{z})^0]\right) = \log(1) = 0 \\ \log(Z_{t=1}) &= \log\left(\mathbb{E}_{p_{f,\Phi}(\mathbf{z}|\mathbf{x})} [\log p_{\Phi}(\mathbf{x} | \mathbf{z})]\right) = \log p_{f,\Phi}(\mathbf{x}) \end{aligned} \quad (53)$$

Therefore, we obtain the log-marginal likelihood expressed as the Thermodynamic Integral:

$$\log(Z_{t=1}) - \log(Z_{t=0}) = \log p_{f,\Phi}(\mathbf{x}) = \int_0^1 \mathbb{E}_{p_{f,\Phi}(\mathbf{z}|\mathbf{x},t)} [\log p_{\Phi}(\mathbf{x} | \mathbf{z})] dt \quad (54)$$

E.0.6. DISCRETIZING THE THERMODYNAMIC INTEGRAL

Here, t_k denotes the tempering at the k -th index of the schedule, and N_t is the number of temperatures. As derived by Calderhead & Girolami (2009), Eq. 21 then be evaluated using:

$$\log(p_{f,\Phi}(\mathbf{x})) = \frac{1}{2} \sum_{k=1}^{N_t} \Delta t_k (E_{k-1} + E_k) + \frac{1}{2} \sum_{k=1}^{N_t} D_{\text{KL}}(p_{t_{k-1}} || p_{t_k}) - D_{\text{KL}}(p_{t_k} || p_{t_{k-1}}) \quad (55)$$

Where:

$$\begin{aligned} \Delta t_k &= t_k - t_{k-1}, \quad E_k = \mathbb{E}_{p_{f,\Phi}(\mathbf{z}|\mathbf{x},t_k)} [\log(p_{\Phi}(\mathbf{x} | \mathbf{z}))], \\ D_{\text{KL}}(p_{t_{k-1}} || p_{t_k}) &= \mathbb{E}_{p_{f,\Phi}(\mathbf{z}|\mathbf{x},t_{k-1})} \left[\log \left(\frac{p_{f,\Phi}(\mathbf{z} | \mathbf{x}, t_{k-1})}{p_{f,\Phi}(\mathbf{z} | \mathbf{x}, t_k)} \right) \right] \end{aligned} \quad (56)$$

This reflects the trapezium rule for numerical integration, supported by bias correction to provide an estimate of the Riemann integral across t that is especially robust to error. The learning gradient derived from the discretized Thermodynamic Integral is unchanged from the MLE gradient in Eq. 4, as demonstrated under Sec. E.0.7.

E.0.7. LEARNING GRADIENT FOR DISCRETIZED THERMODYNAMIC INTEGRAL AND POWER POSTERIOR PARTITION FUNCTION

We can derive the learning gradient of the discretized Thermodynamic Integral in Eq. 55 by reducing it down into a sum of normalizing constants. Starting from the definitions attributed to the KL divergence terms:

$$\begin{aligned} D_{\text{KL}}(p_{t_{k-1}} || p_{t_k}) &= \mathbb{E}_{p_{f,\Phi}(\mathbf{z}|\mathbf{x},t_{k-1})} \left[\log p_{f,\Phi}(\mathbf{z} | \mathbf{x}, t_{k-1}) - \log p_{f,\Phi}(\mathbf{z} | \mathbf{x}, t_k) \right] \\ \text{and } D_{\text{KL}}(p_{t_k} || p_{t_{k-1}}) &= \mathbb{E}_{p_{f,\Phi}(\mathbf{z}|\mathbf{x},t_k)} \left[\log p_{f,\Phi}(\mathbf{z} | \mathbf{x}, t_k) - \log p_{f,\Phi}(\mathbf{z} | \mathbf{x}, t_{k-1}) \right] \\ &= -\mathbb{E}_{p_{f,\Phi}(\mathbf{z}|\mathbf{x},t_k)} \left[\log p_{f,\Phi}(\mathbf{z} | \mathbf{x}, t_{k-1}) - \log p_{f,\Phi}(\mathbf{z} | \mathbf{x}, t_k) \right] \end{aligned} \quad (57)$$

We can leverage Eq. 12 to quantify the log-difference in terms of the change in likelihood contribution plus some normalization constant:

$$\log p_{f,\Phi}(\mathbf{z} | \mathbf{x}, t_{k-1}) - \log p_{f,\Phi}(\mathbf{z} | \mathbf{x}, t_k) = -\Delta t_k \cdot \log p_{\Phi}(\mathbf{x} | \mathbf{z}) + \log \left(\frac{Z_{t_k}}{Z_{t_{k-1}}} \right) \quad (58)$$

The definitions in Eq. 56 can be used to express the KL divergences in terms of the expected likelihoods:

$$\begin{aligned} \therefore D_{\text{KL}}(p_{t_{k-1}} \| p_{t_k}) &= -\Delta t_k \cdot \mathbb{E}_{p_{f,\Phi}(\mathbf{z}|\mathbf{x},t_{k-1})} \left[\log p_{\Phi}(\mathbf{x} | \mathbf{z}) \right] + \log \left(\frac{Z_{t_k}}{Z_{t_{k-1}}} \right) \\ &= -\Delta t_k \cdot E_{k-1} + \log \left(\frac{Z_{t_k}}{Z_{t_{k-1}}} \right) \end{aligned} \quad (59)$$

$$\begin{aligned} \text{and } D_{\text{KL}}(p_{t_k} \| p_{t_{k-1}}) &= \Delta t_k \cdot \mathbb{E}_{p_{f,\Phi}(\mathbf{z}|\mathbf{x},t_k)} \left[\log p_{\Phi}(\mathbf{x} | \mathbf{z}) \right] - \log \left(\frac{Z_{t_k}}{Z_{t_{k-1}}} \right) \\ &= \Delta t_k \cdot E_k - \log \left(\frac{Z_{t_k}}{Z_{t_{k-1}}} \right) \end{aligned} \quad (60)$$

Substituting back into Eq. 55, we eliminate the expected likelihood terms:

$$\begin{aligned} \frac{1}{2} \sum_{k=1}^{N_t} D_{\text{KL}}(p_{t_{k-1}} \| p_{t_k}) - D_{\text{KL}}(p_{t_k} \| p_{t_{k-1}}) &= -\frac{1}{2} \sum_{k=1}^{N_t} \Delta t_k (E_{k-1} + E_k) - 2 \log \left(\frac{Z_{t_k}}{Z_{t_{k-1}}} \right) \\ \therefore \log(p_{f,\Phi}(\mathbf{x})) &= \frac{1}{2} \sum_{k=1}^{N_t} \Delta t_k (E_{k-1} + E_k) + \frac{1}{2} \sum_{k=1}^{N_t} D_{\text{KL}}(p_{t_{k-1}} \| p_{t_k}) - D_{\text{KL}}(p_{t_k} \| p_{t_{k-1}}) \\ &= \frac{1}{2} \sum_{k=1}^{N_t} \Delta t_k (E_{k-1} + E_k) - \left[\frac{1}{2} \sum_{k=1}^{N_t} \Delta t_k (E_{k-1} + E_k) - 2 \log \left(\frac{Z_{t_k}}{Z_{t_{k-1}}} \right) \right] \\ &= \sum_{k=1}^{N_t} \log \left(\frac{Z_{t_k}}{Z_{t_{k-1}}} \right) = \sum_{k=1}^{N_t} \log(Z_{t_k}) - \log(Z_{t_{k-1}}) \end{aligned} \quad (61)$$

Following a similar method to Sec. E.0.4 we can use Eq. 41 to express the learning gradient attributed to each normalization constant in a simpler manner:

$$\begin{aligned} &\mathbb{E}_{p_{f,\Phi}(\mathbf{z}|\mathbf{x},t_k)} \left[\nabla_{f,\Phi} \log p_{f,\Phi}(\mathbf{z} | \mathbf{x}, t_k) \right] \\ &= \mathbb{E}_{p_{f,\Phi}(\mathbf{z}|\mathbf{x},t_k)} \left[t_k \cdot \nabla_{\Phi} \log p_{\Phi}(\mathbf{x} | \mathbf{z}) + \nabla_f \log p_f(\mathbf{z}) \right] - \nabla_{f,\Phi} \log(Z_{t_k}) = 0 \\ \therefore \nabla_{f,\Phi} \log(Z_{t_k}) &= \mathbb{E}_{p_{f,\Phi}(\mathbf{z}|\mathbf{x},t_k)} \left[t_k \cdot \nabla_{\Phi} \log p_{\Phi}(\mathbf{x} | \mathbf{z}) + \nabla_f \log p_f(\mathbf{z}) \right] \end{aligned} \quad (62)$$

Telescoping the sum in Eq. 61, and noting that $k = 1$ corresponds to the power posterior equaling the prior, and $k = N_t$ to the posterior, Eq. 61 yields KAEM's learning gradient:

$$\begin{aligned} \nabla_{f,\Phi} \log(p_{f,\Phi}(\mathbf{x})) &= \sum_{k=1}^{N_t} \nabla_{f,\Phi} \log(Z_{t_k}) - \nabla_{f,\Phi} \log(Z_{t_{k-1}}) \\ &= \nabla_{f,\Phi} \log(Z_{t_{N_t}}) - \nabla_{f,\Phi} \log(Z_{t_0}) \\ &= \mathbb{E}_{p_{f,\Phi}(\mathbf{z}|\mathbf{x})} \left[\nabla_f \log p_f(\mathbf{z}) + \nabla_{\Phi} \log p_{\Phi}(\mathbf{x} | \mathbf{z}) \right] \\ &\quad - \underbrace{\mathbb{E}_{p(\mathbf{z}|f)} \left[\nabla_f [\log p_f(\mathbf{z})] \right]}_{=0 \text{ (Eq. 41)}}. \end{aligned} \quad (63)$$

F. Supplementary experiment details

F.1. Hyperparameters tables

Table 4. Hyperparameters for NIST datasets in Sec. 4.2.

EBM Prior		
layer_widths	p, q	40, 81
spline_type	(-)	RBF
spline_activation	(-)	Relu
layer_norm	(-)	false
spline_degree	d	3
grid_size	N_{grid}	20
grid_update_ratio	α_{grid}	0.05
Initial grid_range (before grid updating)	$[z_{\min}, z_{\max}]$	Uniform: [0, 1] Gaussian: [-1.5, 1.5] No ref.: [-1.2, 1.2]
Spline basis ε init.	ε	0.1
Spline basis μ scaling	μ	1.0
Basis activation scaling	σ_b	1.0
Basis spline scaling	σ_s	1.0
Initial basis param.	τ_0	1.0
Train basis param.	$\tau_{\text{trainable}}$	true
GaussQuad_nodes	N_{quad}	200
Use mixture prior	(-)	false
KAN Likelihood		
hidden_widths	$q, 2q + 1$	81, 162
All other KAN hparams	Identical to EBM Prior	
generator_noise	σ_{ε}	0.1
generator_variance	σ_{llhood}	0.1
output_activation	σ_{act}	sigmoid
Importance sampling resampler	resampler	residual
ESS threshold	γ	0.5
Grid updating		
update_prior_grid	(-)	true
update_llhood_grid	(-)	true
num_grid_updating_samples	(-)	100
grid_update_frequency	(-)	100
grid_update_decay	(-)	0.999
Training		
batch_size	N_x	100
importance_sample_size	N_s	100
Training examples	N_{train}	50,000
Testing examples	N_{test}	100
num_generated_samples	(-)	3,000
Number of epochs	N_{epochs}	10
eps	ϵ	0.001
Optimizer		
type	(-)	adam
learning_rate	η_{LR}	0.001
betas	(-)	(0.9, 0.999)

Kolmogorov-Arnold Energy Models

Table 5. Hyperparameters for SVHN and CelebA in Sec. 4.2.

EBM Prior		
layer_widths	p, q	See Sec. 3.1
spline_type	(-)	Morlet Wavelet
spline_activation	(-)	None
layer_norm	(-)	false
spline_degree	d	3
grid_size	N_{grid}	N/A
grid_update_ratio	α_{grid}	N/A
Initial grid_range (before grid updating)	$[z_{\min}, z_{\max}]$	$[-1.5, 1.5]$
Spline basis ε init.	ε	0.1
Spline basis μ scaling	μ	1.0
Basis activation scaling	σ_b	1.0
Basis spline scaling	σ_s	1.0
Initial basis param.	τ_0	1
Train basis param.	$\tau_{\text{trainable}}$	true
GaussQuad_nodes	N_{quad}	200
Use mixture prior	(-)	true
KAN Likelihood		
cnn_widths	(-)	See Sec. 3.1
All other KAN hparams	N/A, an MLP CNN was used	
generator_noise	σ_{ε}	0.25
generator_variance	σ_{ε}	0.25
output_activation	σ_{act}	sigmoid
Importance sampling resampler	resampler	Not used
ESS threshold	γ	N/A
VGG16 perceptual loss scale, perceptual_scale	(-)	N/A
Grid updating		
update_prior_grid	(-)	false
update_llhood_grid	(-)	false
num_grid_updating_samples	(-)	100
grid_update_frequency	(-)	100
grid_update_decay	(-)	0.999
Training		
batch_size	N_x	100
importance_sample_size	N_s	N/A
Training examples	N_{train}	20,000
Testing examples	N_{test}	100
num_generated_samples	(-)	20,000
Number of epochs	N_{epochs}	200
eps	ϵ	0.001
Use VGG16 perceptual loss, use_perceptual_loss	(-)	false
Optimizer		
type	(-)	adam
learning_rate	η_{LR}	0.0002
betas	(-)	(0.9, 0.999)
POSTERIOR LANGEVIN		
iters	N_{local}	40
step_size	η	0.005
THERMODYNAMIC INTEGRATION		
iters	N_{local}	(see posterior langevin)
num_temps	N_t	5
Initial exponent in power law schedule	p_{start}	2
Final exponent in power law schedule	p_{end}	0.5
Number of cosine cycles	N_{cycles}	0

F.2. SVHN & CelebA Architectures

F.2.1. KAEM ARCHITECTURES

Table 6. The dense Morlet wavelet KAN network used as the mixture prior model

Layer	Operation	Output Dim.
Input	Sample z	$P = 40$
Energy functions	Dense(40)	$Q = 81$

sizes=[$n_z = 40, 2n_z + 1 = 81$]

 Table 7. CNN Generator Architecture for SVHN (32×32)

Layer	Operation	Output Shape	Stride
Input	Latent vector z reshaped	$1 \times 1 \times q$	–
1	4×4 convT(256), LeakyReLU	$4 \times 4 \times 256$	1
2	4×4 convT(128), LeakyReLU	$8 \times 8 \times 128$	2
3	4×4 convT(64), LeakyReLU	$16 \times 16 \times 64$	2
4	4×4 convT(3), Sigmoid	$32 \times 32 \times 3$	2

Config: kernel=4,4,4,4 strides=1/2/2/2, paddings=0/1/1/1, activation=LeakyReLU, batchnorm=False

 Table 8. CNN Generator Architecture for CelebA (64×64)

Layer	Operation	Output Shape	Stride
Input	Latent vector z reshaped	$1 \times 1 \times q$	–
1	4×4 convT(512), LeakyReLU	$4 \times 4 \times 512$	1
2	4×4 convT(256), LeakyReLU	$8 \times 8 \times 256$	2
3	4×4 convT(128), LeakyReLU	$16 \times 16 \times 128$	2
4	4×4 convT(64), LeakyReLU	$32 \times 32 \times 64$	2
5	4×4 convT(3), Sigmoid	$64 \times 64 \times 3$	2

Config: kernel=4,4,4,4,4 strides=1/2/2/2/2, paddings=0/1/1/1/1, activation=LeakyReLU, batchnorm=False

F.2.2. BASELINE VAE ARCHITECTURES

 Table 9. VAE Encoder Architecture for SVHN (32×32)

Layer	Operation	Output Shape	Stride
Input	Image x	$32 \times 32 \times 3$	–
1	4×4 conv(64), LeakyReLU	$16 \times 16 \times 64$	2
2	4×4 conv(128), LeakyReLU	$8 \times 8 \times 128$	2
3	4×4 conv(256), LeakyReLU	$4 \times 4 \times 256$	2
4	Flatten + FC	$\mu, \log \sigma^2 \in \mathbb{R}^{81}$	–

Config: kernels=4,4,4, strides=2/2/2, paddings=1/1/1, latent_dim=81, batchnorm=False

Kolmogorov-Arnold Energy Models

Table 10. VAE Decoder Architecture for SVHN (32×32)

Layer	Operation	Output Shape	Stride
Input	Latent vector z	81	–
1	FC + Reshape	$4 \times 4 \times 256$	–
2	4×4 convT(128), LeakyReLU	$8 \times 8 \times 128$	2
3	4×4 convT(64), LeakyReLU	$16 \times 16 \times 64$	2
4	4×4 convT(3), Sigmoid	$32 \times 32 \times 3$	2

Config: kernels=4,4,4, strides=2/2/2, paddings=1/1/1, latent_dim=81, batchnorm=False

Table 11. VAE Encoder Architecture for CelebA (64×64)

Layer	Operation	Output Shape	Stride
Input	Image x	$64 \times 64 \times 3$	–
1	4×4 conv(64), LeakyReLU	$32 \times 32 \times 64$	2
2	4×4 conv(128), LeakyReLU	$16 \times 16 \times 128$	2
3	4×4 conv(256), LeakyReLU	$8 \times 8 \times 256$	2
4	4×4 conv(512), LeakyReLU	$4 \times 4 \times 512$	2
5	Flatten + FC	$\mu, \log \sigma^2 \in \mathbb{R}^{81}$	–

Config: kernels=4,4,4,4, strides=2/2/2/2, paddings=1/1/1/1, latent_dim=81, batchnorm=False

Table 12. VAE Decoder Architecture for CelebA (64×64)

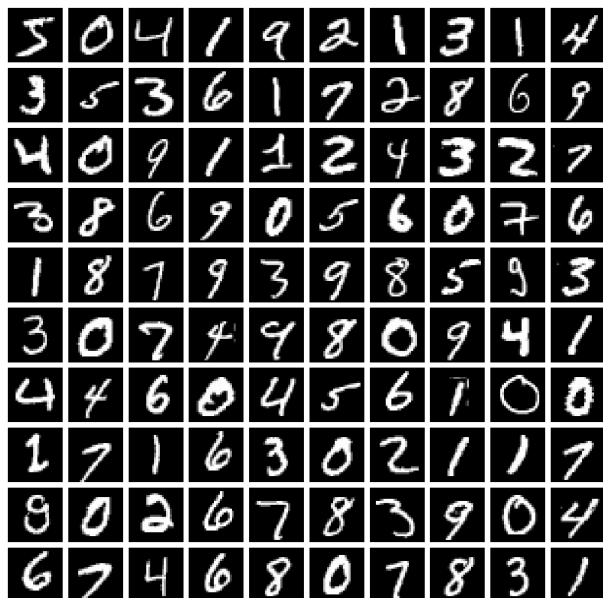
Layer	Operation	Output Shape	Stride
Input	Latent vector z	81	–
1	FC + Reshape	$4 \times 4 \times 512$	–
2	4×4 convT(256), LeakyReLU	$8 \times 8 \times 256$	2
3	4×4 convT(128), LeakyReLU	$16 \times 16 \times 128$	2
4	4×4 convT(64), LeakyReLU	$32 \times 32 \times 64$	2
5	4×4 convT(3), Sigmoid	$64 \times 64 \times 3$	2

Config: kernels=4,4,4,4, strides=2/2/2/2, paddings=1/1/1/1, latent_dim=81, batchnorm=False

G. Generated images

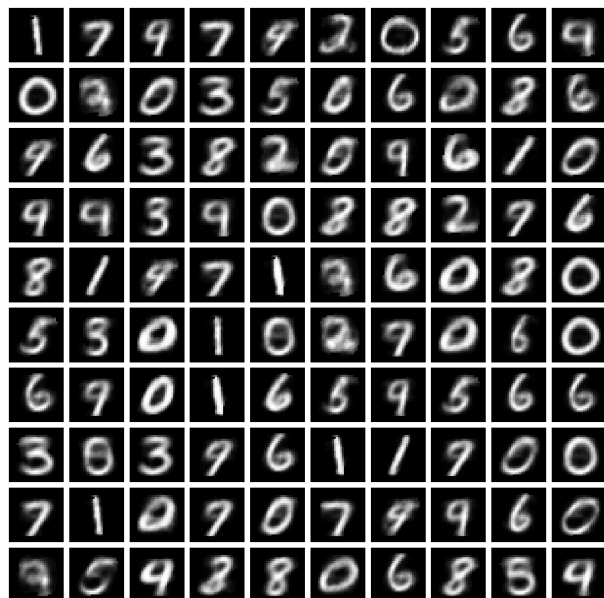
G.1. MNIST & FMNIST

MNIST - Real Images (Reference)



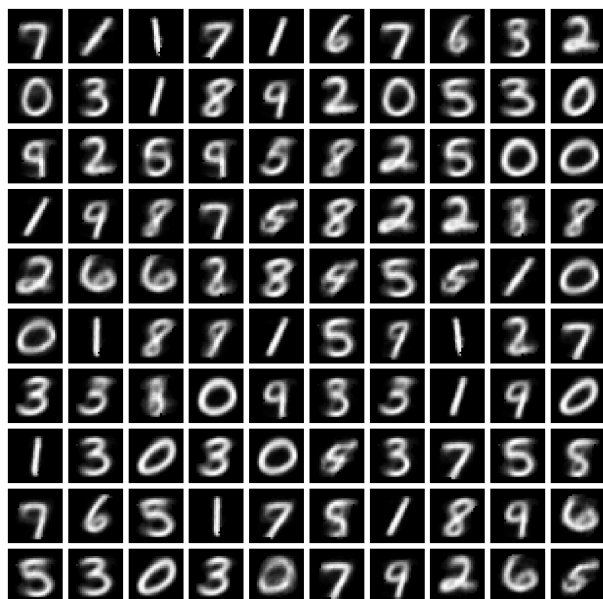
(a) Real samples

MNIST - EBM - RBF



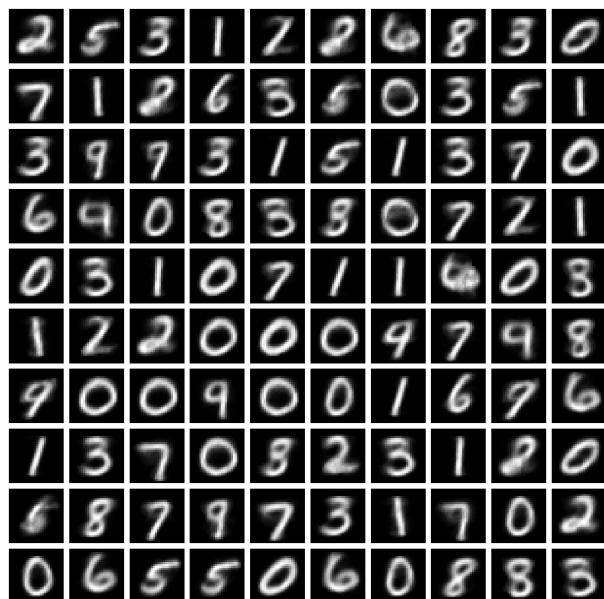
(b) No ref. prior

MNIST - $\mathcal{N}(\mathbf{0}, \mathbf{1})$ - RBF



(c) Gaussian ref. prior

MNIST - $\mathcal{U}(\mathbf{0}, \mathbf{1})$ - RBF



(d) Uniform ref. prior

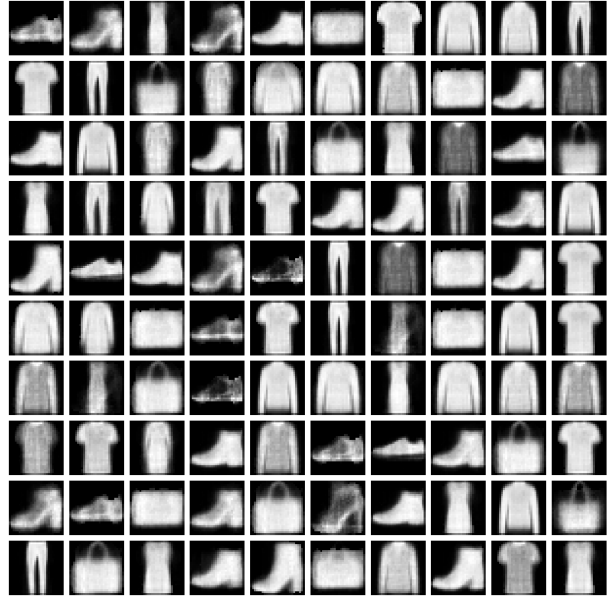
Figure 13. Generated MNIST samples

FMNIST - Real Images (Reference)



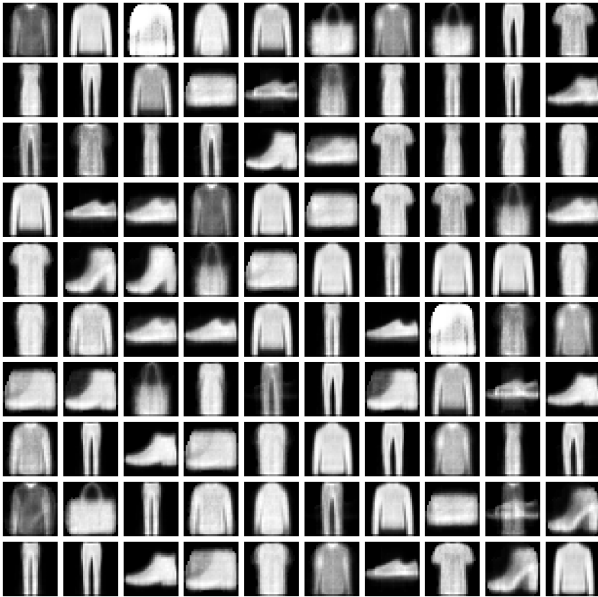
(a) Real samples

FMNIST - EBM - RBF



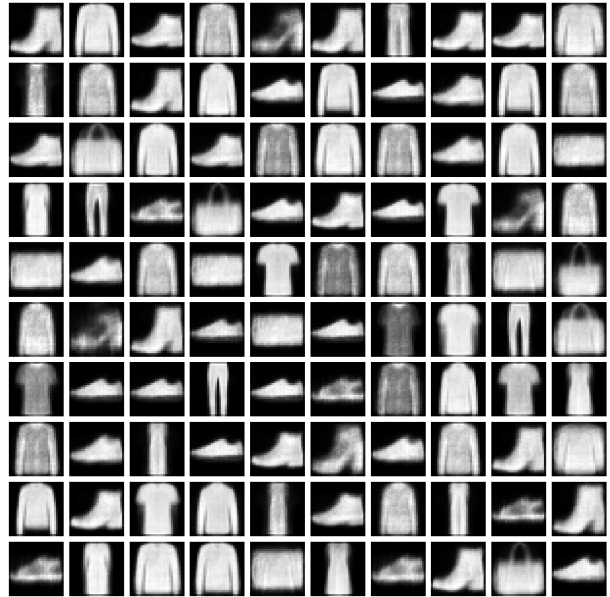
(b) No ref. prior

FMNIST - $\mathcal{N}(\mathbf{0}, \mathbf{1})$ - RBF



(c) Gaussian ref. prior

FMNIST - $\mathcal{U}(\mathbf{0}, \mathbf{1})$ - RBF



(d) Uniform ref. prior

Figure 14. Generated FMNIST samples

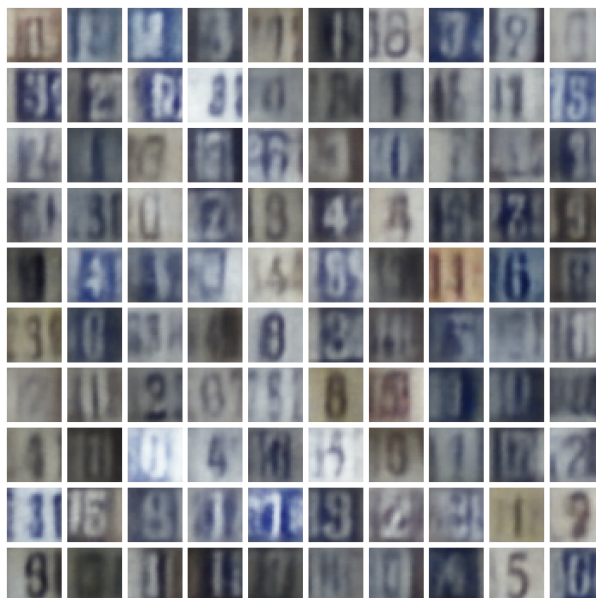
G.2. SVHN & CelebA

SVHN - Real Images (Reference)



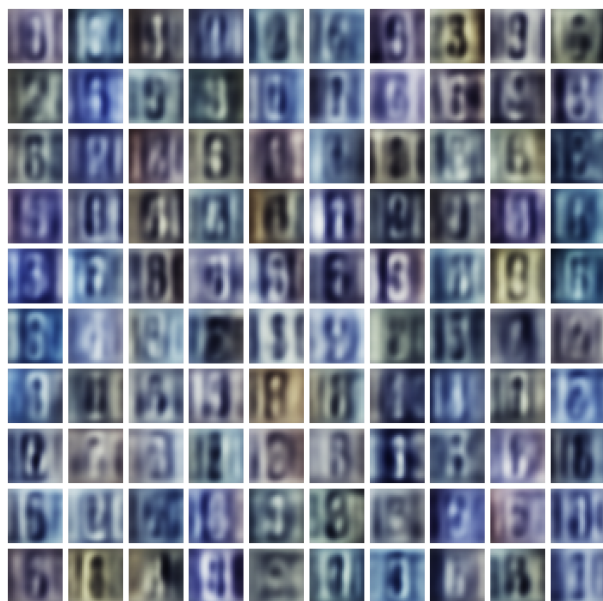
(a) Real samples

SVHN - Baseline - VAE



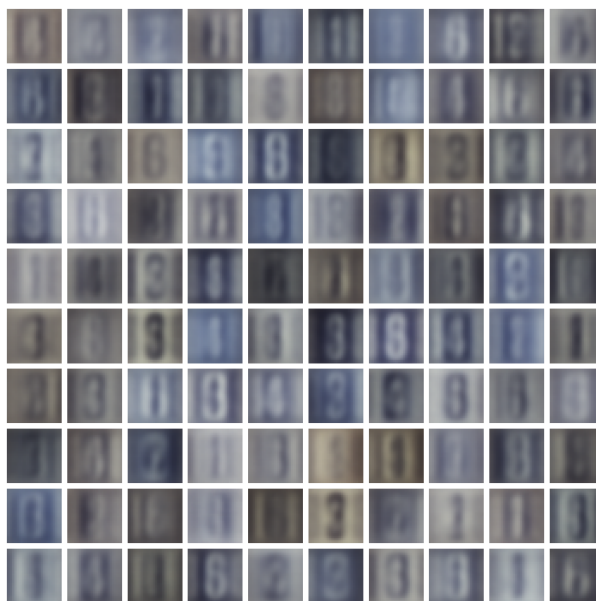
(b) VAE baseline

SVHN - Vanilla - ULA - mixture



(c) MLE-trained with ULA sampling

SVHN - Thermodynamic - ULA - mixture



(d) Thermo-trained with population-based ULA

Figure 15. Generated SVHN samples

CELEBA - Real Images (Reference)



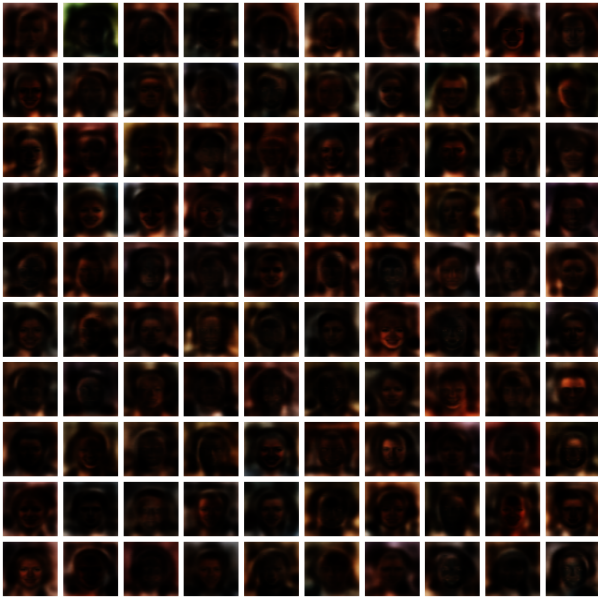
(a) Real samples

CELEBA - Baseline - VAE



(b) VAE baseline

CELEBA - Vanilla - ULA - mixture



(c) MLE-trained with ULA sampling

CELEBA - Thermodynamic - ULA - mixture



(d) Thermo-trained with population-based ULA

Figure 16. Generated CelebA samples

H. Smaller RBF Experiment

To investigate how hyperparameter choice affects sample quality, we conducted a smaller-scale supplementary experiment using RBF bases. Most hyperparameters were kept consistent with Tab. 5, except for using RBF bases with ReLU base activation and 20 grid points, alongside a smaller additive noise variance of $\sigma_{\text{noise}} = 0.1$ and a larger posterior sampling step

size, $\eta = 0.01$. Training was conducted for 40 epochs with 20,000 training examples and a batch size of $N = 50$ (i.e., only 16,000 parameter updates).

The grid updating procedure proposed by Liu et al. (2024) was applied periodically, starting at once every 100 parameter updates with a frequency decay of 0.999, using 100 samples to update the prior’s domain based on regions explored by ULA.

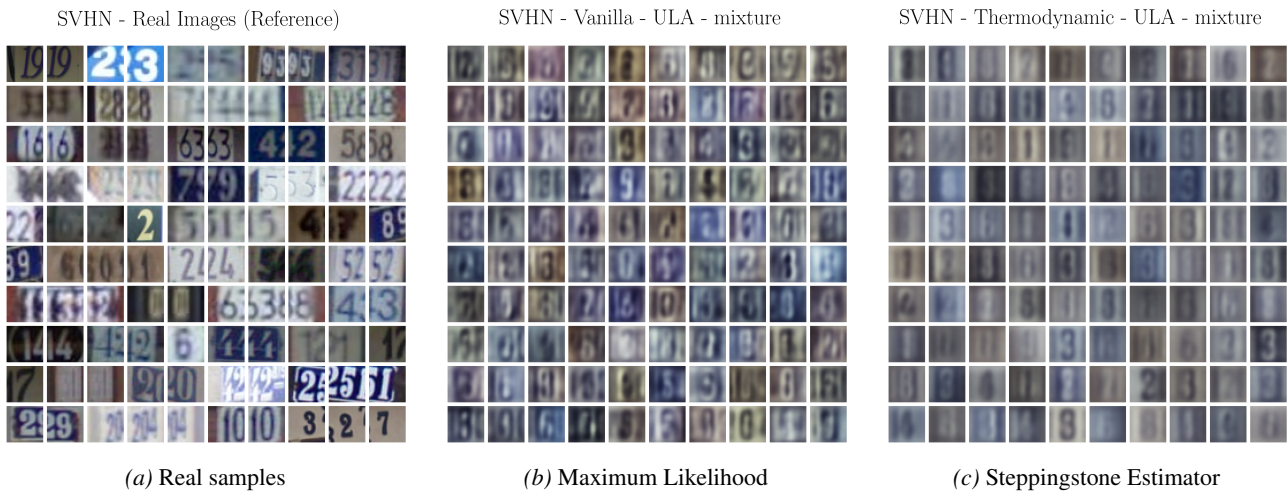
Effectively unbiased metrics were collected using regression on sample sizes 1000, 1200, 1400, 1600, 1800, 2000, 2200, 2400, 2600, 2800, 3000 (i.e., significantly smaller than those used in the main experiment). Regression statistics, (standard errors and R^2), were not collected for this supplementary experiment.

Model	$\overline{\text{FID}}_\infty$	$\overline{\text{KID}}_\infty$
MLE	78.41	0.0627
Thermo	165.79	0.1608

Table 13. SVHN (32×32), RBF experiment.

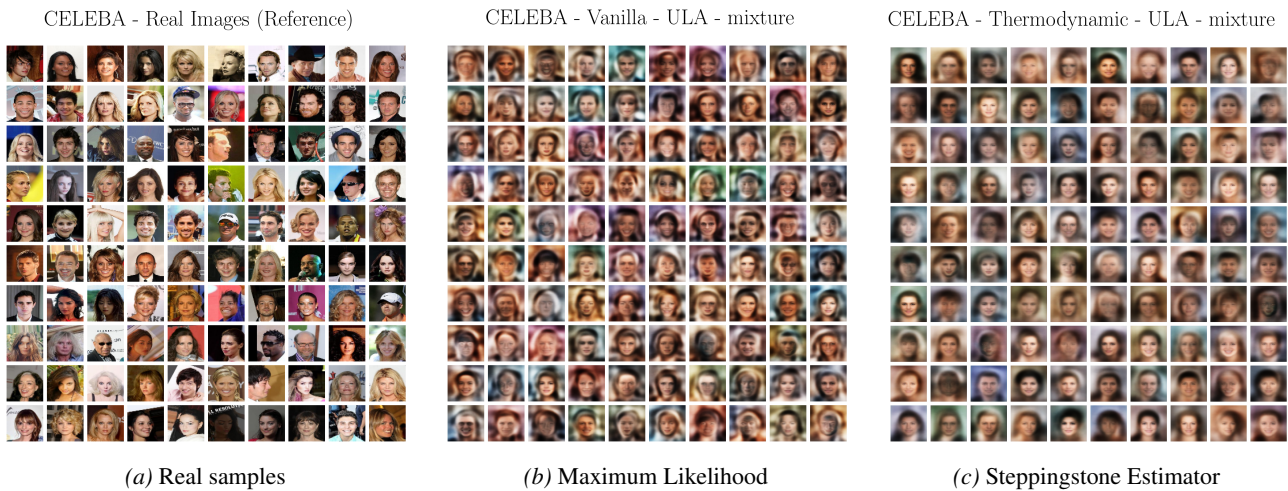
Model	$\overline{\text{FID}}_\infty$	$\overline{\text{KID}}_\infty$
MLE	130.05	0.1427
Thermo	150.25	0.1637

Table 14. CelebA (64×64), RBF experiment.



(a) Real samples (b) Maximum Likelihood (c) Steppingstone Estimator

Figure 17. Generated SVHN (32×32) samples using RBF bases with mixture prior architecture



(a) Real samples (b) Maximum Likelihood (c) Steppingstone Estimator

Figure 18. Generated CelebA (64×64) samples using RBF bases with mixture prior architecture

Algorithm 3 Residual resampling (ESS-triggered)

Require: Latrnt samples $\{z^{(s)}\}_{s=1}^N$ with normalized likelihood-based weights $\{w_s\}_{s=1}^N$ ($\sum_{s=1}^N w_s = 1$); threshold fraction $\gamma \in (0, 1]$.

Ensure: Resampled $\{\tilde{z}^{(i)}\}_{i=1}^N$ and weights $\{\tilde{w}_i\}_{i=1}^N$.

```

1: ESS gating:  $\text{ESS} \leftarrow \left( \sum_{s=1}^N w_s^2 \right)^{-1}$ .
2: if  $\text{ESS} \geq \gamma N$  then
3:   for  $i = 1$  to  $N$  do
4:      $\tilde{z}^{(i)} \leftarrow z^{(i)}$ 
5:      $\tilde{w}_i \leftarrow w_i$ 
6:   end for
7:   return  $\{(\tilde{z}^{(i)}, \tilde{w}_i)\}_{i=1}^N$  {no resampling}
8: end if
9: Integer replication and residual mass:
10: for  $s = 1$  to  $N$  do
11:    $r_s \leftarrow \lfloor N w_s \rfloor$ 
12:    $m_s \leftarrow N w_s - r_s$  {residual mass}
13: end for
14:  $R \leftarrow N - \sum_{s=1}^N r_s$  {# residual draws}
15: Initialize index list:  $\mathcal{I} \leftarrow []$ .
16: for  $s = 1$  to  $N$  do
17:   Append  $s$  to  $\mathcal{I}$  exactly  $r_s$  times
18: end for  $\{|\mathcal{I}| = N - R\}$ 
19: if  $R > 0$  then
20:   Normalize residual weights:
21:   for  $s = 1$  to  $N$  do
22:      $\bar{w}_s \leftarrow m_s / R$ 
23:   end for
24:   Build CDF:  $C_0 \leftarrow 0$ 
25:   for  $s = 1$  to  $N$  do
26:      $C_s \leftarrow C_{s-1} + \bar{w}_s$ 
27:   end for
28:   Draw remaining  $R$  indices (multinomial):
29:   for  $i = 1$  to  $R$  do
30:     Sample  $u \sim \text{Unif}(0, 1)$ 
31:     Find smallest  $k^*$  such that  $C_{k^*} \geq u$ 
32:     Append  $k^*$  to  $\mathcal{I}$ 
33:   end for
34: end if
35: Resample and reset weights:
36: for  $i = 1$  to  $N$  do
37:    $\tilde{z}^{(i)} \leftarrow z^{(\mathcal{I}_i)}$ 
38:    $\tilde{w}_i \leftarrow 1/N$ 
39: end for
40: return  $\{(\tilde{z}^{(i)}, \tilde{w}_i)\}_{i=1}^N$ .
    
```
